Research Report

Architecture and organization of mouse posterior parietal cortex relative to extrastriate areas

Karoline Hovde*, Michele Gianatti, Menno P. Witter, and Jonathan R. Whitlock*

Kavli Institute for Systems Neuroscience, Norwegian University of Science and Technology, NO-7489 Trondheim, Norway

*To whom correspondence should be addressed:

e-mail: karoline.hovde@ntnu.no

e-mail: whitlock@ntnu.no

Running title: Mouse posterior parietal cortex

No. text pages: 39; Abstract: 207 words (limit 250)

No. figures: 7

Supplementary Material: 3 figures, 2 tables, 1 list

KEYWORDS: cortico-cortical connectivity, tract tracing, parietal cortex, frontal cortex, pre-frontal cortex, visual cortex, anatomy

ABSTRACT

The posterior parietal cortex (PPC) is a multifaceted region of cortex, contributing to several cognitive processes including sensorimotor integration and spatial navigation. Although recent years have seen a considerable rise in the use of rodents, particularly mice, to investigate PPC and related networks, a coherent anatomical definition of PPC in the mouse is still lacking. To address this, we delineated the mouse PPC using cyto- and chemoarchitectural markers from Nissl-, parvalbumin- and muscarinic acetylcholine receptor M2-staining. Additionally, we performed bilateral triple anterograde tracer injections in primary visual cortex (V1) and prepared flattened tangential sections from one hemisphere and coronal sections from the other, allowing us to co-register the cytoarchitectural features of PPC with V1 projections. This revealed that extrastriate area A was largely contained within lateral PPC, that medial PPC overlapped with the anterior portion of area AM, and that anterior RL overlapped partially with area PtP. Furthermore, triple anterograde tracer injections in PPC showed strong projections to associative thalamic nuclei as well as higher visual areas, orbitofrontal, cingulate and secondary motor cortices. Retrograde circuit mapping with rabies virus further showed that all cortical connections were reciprocal. These combined approaches provide a coherent definition of mouse PPC that incorporates laminar architecture, extrastriate projections, thalamic, and cortico-cortical connections.

INTRODUCTION

The posterior parietal cortex (PPC) is one of the major associational cortical areas in the brain. Across mammalian species, it receives inputs from virtually all sensory modalities, frontal motor areas and prefrontal cortex (Reep *et al.*, 1994; Krubitzer, 1995; Wise *et al.*, 1997; Stepniewska *et al.*, 2016), and it supports a variety of cognitive functions, including sensorimotor transformations, spatial processing, decision-making and movement planning. For several decades, the monkey has served as the premiere model for investigating the behavioral and neurophysiological contributions of PPC, and while PPC in rodents is substantially smaller and less differentiated, recent years have seen an increase in the use of rats and mice. This has been motivated in part by the fact that rodents can be trained to perform a variety of highly specific, PPC-dependent tasks in real world and virtual reality settings (Nitz, 2006; Harvey *et al.*, 2012; Raposo *et al.*, 2012; Whitlock *et al.*, 2012; Brunton *et al.*, 2013; Wilber *et al.*, 2014b; Goard *et al.*, 2016; Hwang *et al.*, 2017). The advantages of mice in particular include their genetic tractability and compatibility with large-scale recording and imaging techniques, leading to their widespread usage to study population coding and circuit function in every major sector of cortex, including PPC. Despite the popularity of the mouse for studying parietal cortex, however, there is little consensus on a coherent anatomical definition of PPC in the mouse, which is problematic because it complicates the interpretation of the wealth of new data.

As with rats, PPC in the mouse is located between visual and somatosensory cortices (Paxinos & Franklin, 2012), and the existing data suggests that it has similar patterns of cortico-cortical and thalamic connectivity (Kolb & Walkey, 1987; Reep *et al.*, 1994; Harvey *et al.*, 2012; Oh *et al.*, 2014; Wilber *et al.*, 2014a; Olsen & Witter, 2016). More detailed aspects of mouse PPC

anatomy, including the boundaries which distinguish it from neighboring areas, its laminar organization and chemoarchitectural profile remain ill-defined. Recent strategies for targeting PPC in mice have therefore relied either on functionally mapping extrastriate areas (Olavarria *et al.*, 1982) near PPC, or on stereotactic coordinates followed by post-hoc histological comparison to one of several reference atlases (e.g. (Krieg, 1946; Paxinos & Franklin, 2012; Oh *et al.*, 2014, http://connectivity.brain-map.org). These conventions may yield consistent recording locations within a study, but hamper the comparison of PPC across studies since they are based on different labeling methodologies and unrelated nomenclatures.

We sought to resolve these discrepancies by first delineating mouse PPC using cytoarchitectural and laminar criteria obtained from Nissl-, parvalbumin (PV)-, and type-2 muscarinic acetylcholine receptor (M2AChR)-immunostained coronal sections. We next performed bilateral, triple anterograde tracer injections in mouse V1 as in earlier studies (Montero, 1993; Wang & Burkhalter, 2007), and prepared flattened sections from one hemisphere and coronal sections of the other. By labeling extrastriate projections in both flattened and coronal planes, and by comparing these alongside interleaved, annotated Nissl- and M2AChR-stained coronal sections, we located the mouse PPC with respect to the major projections from V1. Based on these coordinates, we performed triple anterograde tracer injections in PPC, revealing a previously undescribed topography in parietal output to higher visual areas. Additional monosynaptic retrograde tracing with rabies virus showed that the inputs to PPC largely matched that described in rats.

MATRIALS AND METHODS

A total of 24 adult C57BL/6JBomTac mice (24-35g, Taconic) were used in the study. Twenty-three were injected with tracers, of which 12 received injections in V1, and 11 were injected in PPC. Of these, 10 animals were excluded due to poor tracer uptake, transport, or off-target injections. Nine animals were used for anterograde tracing, and four animals were used for retrograde tracing, and one mouse was used for the architectural study (see Supplementary Table 1 for full listing). Mice were housed in separate cages with free access to water and food, and were kept on a reversed light-dark cycle. All surgical procedures were approved by the Norwegian Food Safety Authority as well as the local Animal Welfare Committee of the Norwegian University of Science and Technology, and followed the European Communities Council Directive and the Norwegian animal welfare act.

Preparation and delineation of "atlas" brain

A 7 month old female mouse, weighing 30g, was given an overdose of pentobarbital and transcardially perfused using Ringer's solution (0.025% KCl, 0.85% NaCl, 0.02% $NaHCO_3$, pH 6.9) followed by a freshly prepared paraformaldehyde solution (PFA, 4% in 0.125M phosphate buffer, pH 7.4). The brain was carefully removed from the skull and post-fixed in 4% PFA overnight at 4°C. Subsequently, the brain was moved to a cryoprotective solution (2% dimethyl sulfoxide, DMSO in 0.125M phosphate buffer, VWR) and stored again overnight at 4°C before sectioning. The brain was cut in 40µm coronal sections on a freezing microtome (Microm HM430, Thermo Scientific, Waltham, USA) in three equally spaced series. One series was used for Nissl staining, and the

other two were used for immunohistochemistry against PV and M2AChR, respectively. Nissl staining and immunohistochemical procedures were the same for these and the anatomical tracing experiments, and are explained in detail in "Histology and immunochemistry" below. Delineations and cortical field designations for this and all other brains in the study were determined for each hemisphere individually in each analysis.

Anterograde anatomical tracing

The coordinates for initial injections were based on Paxinos and Franklin (2012), and adjusted both to the size of the animal and according to the histology of injection sites in previous animals. All surgeries were performed under isoflurane anesthesia with the animal laying on a heating pad maintaining the body temperature at 37°C. Briefly, the animal was anesthetized in a box pre-filled with isoflurane before being placed in a stereotaxic frame (Kopf Instruments)**.** The analgesics Metacam (5 mg/kg, meloxicam**,** Boehringer Ingelheim Vetmedica) and Temgesic (0.1 mg/kg**,** buprenorphine, Indivior) were injected subcutaneously, as was the local anesthetic Marcain (1-3 mg/kg, bupivacaine, AstraZeneca) where the incision was to be made**.** The head of the animal was shaved, disinfected with 70% ethanol and iodine (Iodine NAF Liniment 2%, Norges Apotekerforening) and a small incision was made along the midline. The skull was cleaned with hydrogen peroxide (H_2O_2, 3%, Norges Apotekerforening) and 0.9% saline, the height of bregma and lambda were measured and adjusted to ensure the skull was levelled, and a craniotomy was made with a high-speed dental drill and 0.25mm burr over the coordinates for injections.

The anterograde tracers used for triple injections were (i) 10 KD biotinylated dextran amine (BDA, Dextran, Biotin, 10,000 MW, Lysine Fixable (BDA-10,000), Thermo Fisher Scientific Cat. No. D1956, RRID:AB_2307337 in 5% solution in 0.125 M phosphate buffer) *or* Dextran, Alexa Fluor™ 647 (ThermoFisher, 10,000 MW, Anionic, Fixable, Catalog number D22914), (ii) Dextran, Alexa Fluor™ 488 (ThermoFisher, 10,000 MW, Anionic, Fixable, Catalog number D22910) and (iii) Dextran, Alexa Fluor™ 546 (ThermoFisher, 10,000 MW, Anionic, Fixable, Catalog number D22911). Tracers were injected iontophoretically by applying pulses of positive DC-current (6s on/off alterations, 6μA) for 10 min using glass micropipettes (20μm tip, Harvard apparatus, 30-0044). In later experiments BDA replaced Dextran, Alexa Fluor™ 647 due to better transport and stronger signal. Different mice were used for injections in V1 (five animals) and PPC (four animals; see Table 1). Injections in V1 were spaced 0.3mm apart beginning 2.30mm lateral of the midline, immediately anterior to the transverse sinus. The injections in PPC were spaced 0.37mm apart, beginning 1.25mm lateral from of the midline and -1.90mm posterior to bregma. Following the injections, the craniotomy was filled with Venus Diamond Flow (Kulzer, Mitsui chemical group), the skull was cleaned with saline, and the wound was stitched and disinfected with iodine. Animals were then transferred to a heating chamber until awake and active, before being moved back to its home cage. Post-operative pain management included Metacam (5 mg/kg) 12 hours post-surgery and, if deemed necessary, 24 hours post-surgery.

Rabies tracing

Injections were made into PPC (B-2.00, L+1.50, D-0.50) following the general surgical procedure as described above (see Table 1 for injection details across animals). For the representative case, 300nl helper virus (AAV1.CamKII0.4.Cre.SV40 + AAV5-syn-FLEX-splitTVA-EGFP-B19G, in a 1:1 ratio; Cre virus from U. Penn Vector Core; TVA virus was a generous gift from the lab of Cliff Kentros) was injected using glass capillaries (World Precision Instruments (WPI), Cat. No. 4878), a Nanoliter2010 injector (WPI) and a Nanoliter2000 pump (WPI), with the glass tip left in place 10 min after the injection. 12 days later, 230nl of rabies virus (EnvA-pseudotyped SAD-DeltaG-mCherry; gift from Kentros lab) was injected in the same location, and the animal was kept alive for 11 days before perfusion.

Tissue collection and preparation

Animals receiving anterograde tracers were perfused one week after the injections. They were given an overdose of pentobarbital and perfused transcardially with Ringer's solution (0.025% KCl, 0.85% NaCl, 0.02% $NaHCO_3$, pH 6.9) followed by freshly prepared paraformaldehyde solution (PFA, Sigma-Aldrich AS, 1% in 0.125M phosphate buffer, pH 7.4). For brains with bilateral tracer injections, the left hemisphere was flattened and the right hemisphere was cut coronally (see below). Such brains were carefully removed from the skull and kept in a container with PFA (1%). Within one hour of the perfusion, the brain was cut in two along the midline to prepare coronal sections of the right hemisphere and tangential sections through flattened tissue (flat maps) from the left hemisphere. Brains with unilateral anterograde tracer injections and brains that received

rabies injections were perfused and post-fixed with 4% PFA and always cut in the coronal plane (see below).

Coronal sections

Coronal sections were prepared from brains that received (i) bilateral anterograde tracer injections, (ii) unilateral anterograde injections, or (iii) rabies injections. For bilateral injections, coronal sections were always made from the right hemisphere. In all cases, brains were carefully removed from the skull following perfusions and transferred to a screw-top vial containing PFA (4%, 0.125M phosphate buffer, pH 7.4), post-fixed overnight at 4°C and transferred to cryoprotective solution (2% DMSO in 0.125M phosphate buffer) the next day, and again stored overnight at 4°C. The hemisphere was then cut in 40µm coronal sections on a freezing microtome (see above) in three equally spaced series. The first series was mounted directly onto Superfrost Plus microscope slides (Gergard Menzel GmbH, Braunschweig, Germany), dried overnight on a heating pad, and used for Nissl staining. Series two and three were each stored in cryoprotective solution at -20°C, and later used for visualizing anterograde tracers or rabies, and the other for immunohistochemistry against M2AChR.

Tangential flattened sections

The left hemisphere was flattened to make “flat maps” of cortex, which first required that cortex was dissected from the rest of the subcortical structures. This was done by first resting the left hemisphere on the midline with the cortex upwards, and gently pressing the cortex flat. The brain

was next flipped over to expose the midline, and a cut was made in fornix dorsal to the anterior commissure. Two brushes were used to push and separate cerebellum, cortex and the underlying subcortical areas from each other. The brainstem was held down with a brush, while dorsal cortex and hippocampus were pushed away with dissection scissors, and cuts were made at the same time along the white matter. The scissors were held parallel to the cutting plane and special care was taken to not damage ventral hippocampus. The brainstem and cerebellum were cut out and removed. One relief cut was made in cingulate cortex and one ventral to postrhinal cortex to facilitate the unfolding of cortex. The cortex was then placed on a microscope glass covered with parafilm (Laboratory film, Pechiney, plastic Packaging, Chicago)**,** and hippocampus and dorsal cortex were gently unfolded using two brushes. Another covered microscope glass was placed on top of the tissue and the two glasses were taped together. The preparation was placed in a container with PFA (4%) overnight at 4°C with a glass weight (52g) on top to provide extra pressure. The following day, the flattened tissue was removed from the microscope glasses and kept in a screw-top container with 2% DMSO in 0.125M phosphate buffer overnight at 4°C. One day later, the brain was mounted onto a freezing microtome stage using a sucrose solution (20%) with dorsal cortex facing down, and 50µm thick sections of flattened cortex were cut and collected in one tube containing 2% DMSO in 0.125M phosphate buffer. The sections were first used for studying projections from V1 to extrastriate areas in flat maps, and were stained subsequently with DAB against M2AChR for delineation purposes (as described in the following section). We defined all cortical boundaries based on myeloarchitecture and M2AChR staining in each hemisphere individually.

Histology and immunochemistry

Nissl staining

Series one from the right hemisphere was stained with cresyl violet (Sigma-Aldrich, St. Louis, MO). Briefly, the sections were dehydrated in increasing percentages of ethanol (50%, 70%, 80%, 90%, 3 x 100%, 10 dips each), cleared in xylene for 2 min, and rehydrated in decreasing concentration of ethanol. The sections were rinsed briefly in running water before being stained with cresyl violet (0.1%) on a shaker for 3 min. The sections were rinsed subsequently in running water and differentiated in an ethanol-acetic acid solution (0.5% acetic acid in 70% ethanol) until optimal staining was achieved. The sections were again dehydrated in increasing percentages of ethanol (as described above), cleared in xylene, and coverslipped with xylene solution (Merck KGaA, Darmstadt, Germany).

Immunohistochemistry against BDA

Series two of the right hemisphere and all sections of the left hemisphere were used for triple-anterograde tracing experiments. Three of the tracers were conjugated with Alexa fluorophores Dextran, Alexa Fluor™ 488, Dextran, Alexa Fluor™ 546 and Alexa Fluor™ 647 whereas BDA was visualized using fluorophore-tagged streptavidin (Thermo Fisher Scientific). This was done by first washing tissue sections 3 × 5 min in 0.125M phosphate buffer (pH 7.4), followed by 3 × 5 min in TBS-Tx (0.5% Triton-X-100, 0.606% Tris(hydroxymethyl)aminomethane, 0.896% NaCl, pH 8.0). The sections were then incubated with primary antibody Streptavidin, Alexa Fluor 633 conjugate (1:400, Thermo Fisher Scientific Cat. No. S-21375, RRID:AB_2313500) in TBS-Tx for 90 min at room

temperature, followed by 3 x 5 min rinsing in Tris buffer 0.606% (Tris(hydroxymethyl)aminomethane, pH 7.6). The tissue sections were then mounted on Menzel-glass slides (Thermo Scientific) using a Tris-gelatin solution (0.2% gelatin in Tris-buffer, pH 7.6), air dried overnight and coverslipped with an entellan-toluene solution the following day.

DAB staining against M2AChR and PV

Tissue sections were stained with 3.3'-Diaminobenzidine tetrahydrochloride (DAB, Sigma-Aldrich, St. Louis, USA) to visualize M2AChR density in series three of the right hemisphere and flat map sections for the anterograde tracer experiments, as well as for series three of the "atlas" brain (Figure 1). DAB staining was also used to visualize PV in series two of the "atlas" brain. The staining procedure for coronal sections was the same across experiments except for flat maps, for which staining was done on the slide, requiring a longer incubation time.

In brief, for immunostaining against M2AChR and PV, sections were first rinsed 2 x 5 min in phosphate buffer (0.125M) followed by 2 x 5 min rinses in TBS-Tx. The sections were incubated with primary antibody (Rat anti-muscarinic acetylcholine receptor M2 monoclonal antibody, unconjugated, clone m2-2-b3, 1:750, Millipore Cat. No. MAB367, RRID:AB_94952; Mouse anti-parvalbumin monoclonal antibody, unconjugated, clone PARV-19, 1:1000, Sigma-Aldrich Cat. No. P3088, RRID:AB_477329) overnight at room temperature. They were then washed 2 x 5 min in TBS-Tx and incubated with mouse absorbed, rabbit-anti-rat secondary antibody (Anti-rat IgG (H+L), 1:300, Vector Laboratories Cat. No. BA-4001, RRID:AB_10015300; Goat anti-mouse IgG, biotin conjugated, 1:200, Sigma-Aldrich Cat. No. B7151, RRID:AB_258604) for 90 min at room

temperature. The sections were then washed 2 x 5 min in TBS-Tx, 2 x 5 min in PB, 2 x 5 min in H_2O_2-metanol solution (0.08%, Sigma-Aldrich), 2 x 5 min TBS-Tx and incubated with a Vector ABC kit (Vector laboratories, Inc., Burlingame, USA) for 90 min at room temperature, per the manufacturer's instructions. Subsequently, the sections were washed 2 x 5 min in TBS-Tx, then 2 x 5 min in Tris-buffer before being incubated with DAB (10 mg in 15mL Tris-buffer, Sigma-Aldrich) at room temperature. Just before the incubation, H_2O_2 (2µL, 30%, Sigma-Aldrich) was added to the DAB solution and it was filtered. The sections were incubated in DAB until they reached the desired color, rinsed in Tris-buffer solution and mounted on Menzel glass slides using a 0.2% gelatin solution. After drying overnight, the slides were coverslipped with an entellan-xylene solution.

Immunohistochemistry against rabies

For brains used for rabies tracing, series two was stained against green fluorescent protein (GFP) and red fluorescent protein (RFP) to visualize the helper virus (AAV1.CamKII0.4.Cre.SV40 + AAV5-syn-FLEX-splitTVA-EGFP-B19G) and the rabies virus (EnvA-pseudotyped SAD-DeltaG-mCherry), respectively. In brief, the tissue was rinsed 3 x 5 min in phosphate buffered saline (PBS, 0.1M, pH 7.4, Sigma-Aldrich) on a shaker at room temperature and rinsed 2 x 10 min in a 0.3% Triton solution (PBS 0.1M and 0.3% Triton). Further, it was incubated with primary antibodies (Rabbit RFP Antibody Pre-adsorbed, 1:1000, Rockland Cat. No. 600-401-379, RRID:AB_2209751**;** Chicken anti-GFP, 1:500, Abcam Cat. No. ab13970, RRID:AB_300798) in a PBS 0.1M + 0.3% Triton + 3% BSA solution on a shaker at 4°C overnight. The tissue was rinsed 2 x 5 min in 0.3% Triton solution and

incubated with secondary antibodies (F(ab)2-goat anti-rabbit IgG (H+L) cross-adsorbed, Alexa Fluor 546, 1:1000, Thermo Fisher Scientific Cat. No. A-11071, RRID:AB_2534115; Goat anti-chicken IgY H&L, Alexa Fluor® 488, 1:1000, Abcam Cat# ab150169, RRID:AB_2636803) in a PBS 0.1M + 0.3% Triton + 3% BSA solution on a shaker at room temperature for one hour. Finally, the tissue was rinsed 2 x 10 min in PBS (0.1M) and mounted on gelatin-coated polysine slides (Thermo Scientific) using PBS (0.1M). After drying for one hour, a Hoechst solution (1:5000 in PBS 0.1M, bisBenzimid H 33258, catalog No. B1155, Sigma-Aldrich) was applied on the sections for 5 min in the dark, the slides were carefully rinsed with PBS and coverslipped with ProLong® Gold antifade reagent (REF P36934, Molecular probes, Life technologies™).

Imaging and analysis

All brain sections were digitized using a Zeiss Axio Scan.Z1 scanner. Selected fluorescent coronal sections and fluorescent flat maps were scanned with a Zeiss confocal microscope (LSM800) in z-stacks and compiled using the max projection function to project all stacks onto a single plane. The scans were edited in Adobe Photoshop CC 2017 and figures were made in Adobe Illustrator CC 2017. Nissl and DAB stained sections were optimized for brightness and contrast. Fluorescent flat maps and coronal sections in Figures 2, 3, 4, 5 and 6 were used for illustration purposes, and were optimized in Adobe Photoshop for brightness and contrast levels for the whole image. Masks were applied to avoid overexposing the injection sites when enhancing the labeling. These were done to reduce background; no labeling was removed, only enhanced for visualization purposes. For Figures 2 and 3, dark field images were taken of the same sections and used as

background underneath the fluorescent sections. Artifacts from blood vessels were removed by making them transparent against the background; see Figures 5, 6, and Supplementary Figures 1-3 for examples of when vascular artifacts were not removed. Descriptions of anterograde and retrograde labeling were intended to be descriptive in nature. We did not quantify the density of labeling or the injections, and therefore do not make assertions about the relative strengths of the connections.

Delineations in Figure 3 were performed on series one of the brains (Nissl) and series three (M2AChR stain). The sections were then overlaid on corresponding fluorescent sections from series two (anterograde or retrograde labeling) in Adobe Illustrator, and the borders where copied onto fluorescent sections. Special care was taken to overlay the sections exactly. Demarcations of cortical and thalamic sub-regions were performed for each experimental hemisphere individually; laminar and chemoarchitectural labeling in coronal sections was in correspondence with Paxinos & Franklin (2012); extrastriate areas in flattened sections were labeled in correspondence with Wang & Burkhalter (2007), and in coronal sections with reference to D'Souza *et al.* (2016). Boundaries for thalamic nuclei were in correspondence with Olsen & Witter (2016). A similar approach was used with Nissl-stained sections directly neighboring the fluorescent sections shown in Figures 5 and 6.

RESULTS

Architectural features of PPC and neighboring areas

Similar to the rat, the mouse PPC lies between primary somatosensory and visual cortices, spanning approximately 600μm anterior-to-posterior, and has distinguishable medial (mPPC), lateral (lPPC) and posterior (PtP) divisions (Paxinos & Watson, 2013; Olsen & Witter 2016). To define precisely the boundaries between PPC and neighboring cortical regions, and to discern parietal sub-areas, we examined laminar architecture using Nissl staining, and chemoarchitectonic patterns using immunostaining against PV and M2AChRs.

Nissl staining. Posterior parietal cortex is bordered anteriorly by secondary motor cortex (M2), lateral to which is a narrow band of primary motor cortex (M1), and even more laterally by primary somatosensory cortex (S1). While cell density is mainly uniform in superficial and deep M2, M1 is conspicuous for a broad layer V with large pyramidal cell bodies, and more homogenous lamination in superficial layers than M2. Lateral to M1, S1 is discernable by prominent lamination and a clearly distinguishable layer IV (Figure 1, top left). Medial to these areas and M2 is agranular retrosplenial cortex (RSA), which contains small, densely packed cell bodies in layer II and a loosely packed layer V that contrasts with the more homogenous distribution of cell bodies across layers in M2. Medial PPC (mPPC; Figure 1, row 2) first emerges at approximately -1.55mm relative to bregma, and is apparent by its homogeneous lamination relative to the neighboring RSA, medially, and S1, laterally. Unlike mPPC, RSA has visibly different cell densities across layers II and III, with layer V having a sparse population of large cell bodies

(Figure 1, rows 1 and 2). Somatosensory cortex is discernable by a well-developed granular layer IV and clearly stratified supragranular and infragranular layers.

The anterior tip of lPPC appears between mPPC and S1 (Figure 1, row 3). Unlike mPPC, lPPC has some discernable lamination between layers II/III and layer V, with layer V being less densely packed than superficial layers. Layer VI of lPPC is also slightly narrower and more densely packed than mPPC. The posterior part of parietal cortex (PtP, from Paxinos & Franklin, 2012) is the most lateral sub-area, and emerges between lPPC and S1 barrel cortex (Figure 1, row 4). Layers II/III of PtP are homogenous with small cells, whereas layer V cells are larger and more sparsely packed. Lateral to PtP is barrel cortex (Figure 1, row 5), which is distinguished by densely packed granular cells in layer IV forming the barrel fields. Posterior to mPPC and lPPC is the medial secondary visual cortex (V2M, Figure 1, row 6), which appears very similar to PPC in Nissl-staining. Considering the proximity and similarity of V2M and PPC with Nissl staining, we found that the emergence of V1, lateral to V2M, was the most useful indicator for being posterior to PPC. Primary visual cortex is characterized by a prominent, granular layer IV that is not present in V2M, and, unlike V2M, V1 is clearly laminated. Similar to S1, V1 contains large pyramidal cells in layer V, and has both superficial and deep cell-sparse zones.

PV staining. In the section anterior to PPC (Figure 1, row 1, middle column), layers III and V of granular retrosplenial cortex (RSG) have very dense staining of cell bodies and neuropil which tapers into RSA and shows a gradual decrease in staining. The border to M2 can be noted by the drop in superficial neuropil staining, which becomes darker again in M1. Moving laterally, S1 has more pronounced stratification, with superficial layer V appearing as a clear stripe between densely stained deeper layers and layer II/III. Just posterior (Figure 1, row 2), the appearance of

mPPC is marked by a salient decrease in PV staining in both cell bodies and the neuropil, which contrasts with the dense staining medially in layers II-V of RSA, and the darker staining in layers IV and V of S1. The neuropil in layer V of lPPC is slightly darker than mPPC (Figure 1, row 3), though both divisions have distinctly less PV staining than S1 and RSA. Laterally, PtP has slightly darker staining in deep layer III and layer V than lPPC (Figure 1, row 4-5), but it is markedly less than the neighboring S1 barrel fields, which have very dark staining in the neuropil of layers IV and V, and more PV+ cells in deeper layers (Figure 1, row 5). In posterior sections, V2M has even less PV staining than the neuropil and cell bodies of PPC. The near-total absence of PV staining is useful for distinguishing V2M from RSA, medially, and V1, laterally, which has a distinct band of staining in the layer V neuropil. Area V2L also has a darkly stained layer V, with weaker staining in superficial layers (Figure 1, row 6).

M2AChR stained sections. Similar to PV staining, RSG shows dense labeling for M2AChRs superficially in layer II as well as in deeper layers. Layer II continues to show prominent staining through RSA, but drops off abruptly at the border with M2 (Figure 2, top row, right column). The superficial staining returns in M1, remains clearly visible laterally through S1, and becomes extremely dense in superficial barrel cortex. Just posterior (Figure 2, row 2, right column), the appearance of mPPC is evidenced by a pronounced decrease in M2AChR staining in superficial layers relative to RSA, medially, and S1, laterally. Posterior to S1 (Figure 1, row 3), the emergence of lPPC is also indicated by a drop in M2AChR staining, and again so with PtP (Figure 1, row 4). The staining in PtP is slightly darker superficially than other parietal areas, but the appearance of S1B, lateral to PtP, is marked by a sharp increase in staining of the superficial barrel fields. Posterior to PPC, V2M virtually lacks M2AChR staining in superficial layers, and is bracketed by

strong staining in RSA and V1 (Figure 1, row 6). Here, the emergence of V1 is marked by strong M2AChR staining directly posterior to lPPC and PtP; again the appearance of V1 is the best indicator of being posterior to all PPC sub-fields in the coronal plane.

Topography of V1 projections in tangential flattened and coronal sections

Topographic maps of V1 projections were obtained in tangential sections from flattened hemispheres containing triple-tracer injections of dextran amines at the posterior pole of V1 (Wang & Burkhalter, 2007). Tracer injections were performed bilaterally in three mice and unilaterally in two, and a representative example of a tangential section through layer IV (Figure 2A) shows the injection sites and clusters of projections to extrastriate areas around the periphery of V1. The relative strengths of these projections were not quantified here, but can be found in previous work (Wang & Burkhalter, 2012). The topography of the projections and delineations of V1 and S1 are with respect to myeloarchitectonic patterns (Figure 2, low-magnification inset) and M2AChRstaining (not shown) from the same sections.

The projections were identified in line with previous studies (Olavarria *et al.*, 1982; Montero, 1993; Wang & Burkhalter, 2007) based on fluorescent labeling, orientation and topographical positioning, and were named using the same nomenclature as these previous studies (see Supplementary Table 2 for a nomenclatural comparison). Similar to their findings, we report a particularly strong projection from V1 to the lateromedial (LM) field, located immediately lateral to V1, and to the laterointermediate (LI) field lateral to LM (Figure 2A). Also consistent with prior reports (Wang & Burkhalter, 2007), LM showed a mirrored medial-to-lateral ordering of the

labeling (Figure 2A), as did the prominently labeled anterolateral (AL) field, just posterior to the S1 barrels. The rostrolateral (RL) area contained a mixture of all tracers and ran parallel to the posterior barrel fields, while the anterior-most labeling was in the anterior (A) field, with labeling from all injections in V1 visible at higher magnifications (Figure 2C, top left). Posterior and medial to area A was the anteromedial (AM) field, with patches of labeling from each tracer stretched along the anterior-posterior axis, followed by the posteromedial (PM) field. While in this case the cyan labeling predominated at low magnification in PM, all tracers were evident at higher magnification (Figure 2C, bottom left).

Similar triple-injections were made in V1 of the right hemisphere, from which coronal sections were cut along the anterior-to-posterior extent of the extrastriate cortex (Figure 2B). Importantly, we verified that projection labeling from contralateral injections was negligible (Supplementary Figure 1), indicating that labeling in coronal or flattened sections came almost entirely from ipsilateral injections. We identified fields in the coronal plane based on their labeling with respect to flat maps, and at levels corresponding to prior descriptions of extrastriate clusters in coronal sections (D'Souza *et al.*, 2016). Consistent with the flat maps, area A was labeled sparsely following injections in V1, whereas the densest projections were to areas LM and AL, both of which exhibited topographically distributed labeling. Each extrastriate area (except LI) is shown at higher magnification in Figure 2C.

Locations of extrastriate areas in relation to PPC

A main goal of this study was to describe the location of extrastriate areas described in classical studies (Olavarria *et al.*, 1982; Olavarria & Montero, 1989; Montero, 1993; Wang & Burkhalter, 2007) in relation to the laminar, cyto- and chemoarchitectural features that distinguish PPC in the mouse. To do this we stacked images of Nissl-stained, annotated PPC sections atop corresponding sections from the same animal with fluorescent V1 projections, and a third series of sections stained for M2AChR (Figure 3). As shown in Figure 3B, at -1.91mm posterior to bregma the entire complement of labeled fibers for area A is contained in lPPC, with no apparent extrastriate labeling in mPPC. Proceeding posteriorly, area A continues to overlap primarily with the lateral areas lPPC and slightly with PtP, while AM overlaps mainly with mPPC and to a lesser extent lPPC (Figure 3C). The bulk of labeling in AM remained in mPPC along the full extent of PPC, while area RL overlapped with PtP and the medial edge of the S1 barrel fields (Figure 3D).

Posterior to PPC, labelling in area AM was contained entirely in V2M (per the nomenclature of Paxinos & Franklin, 2012), and area RL continued to straddle the architectonic boundary between V2L and S1 barrels (Figure 3E). Even more posteriorly, at approximately -2.87mm posterior to bregma, labeling in PM overlapped completely with Paxinos & Franklin's (2012) V2M, whereas V2L totally enveloped AL. We found that the splenium of the corpus callosum was a useful landmark for locating the transition from RL to AL, and that AL emerged at the level where the barrels disappeared in coronal sections. The farther posterior sections (Figure 3G) showed that area LM overlapped completely with posterior V2L, and area LI overlapped with the temporal association area (Te). Although we noted cross-reactivity between antibodies against M2-receptors and BDA labeling (Figures 3F-G), we confirmed that the patterns of M2AChR

labeling in other sections matched staining patterns in tissue preparations without BDA injections (as in Figure 1).

Thalamic and cortical connectivity of mouse PPC

One of the defining features of PPC in rats and other mammals is its connection with associative thalamic nuclei, the lateral posterior (LP), lateral dorsal (LD), and posterior (Po) nucleus (McDaniel *et al.*, 1978; Donoghue & Ebner, 1981; Kolb & Walkey, 1987; Schmahmann & Pandya, 1990; Chandler *et al.*, 1992; Bucci *et al.*, 1999; Padberg & Krubitzer, 2006; Cappe *et al.*, 2007; Olsen & Witter, 2016). Existing evidence indicates that PPC in mice receives input at least from LP (Harvey *et al.*, 2012), so we used coordinates from our prior annotations (Figures 1 and 3) to target triple anterograde tracer injections in PPC (bilaterally in two animals, and unilaterally in two others), and cut the right hemisphere in coronal sections to investigate the patterns of thalamic labeling. In the two bilateral cases, the left hemisphere was used to prepare tangential flattened sections. The locations of PPC projections in all cases were identified using anatomical bounyudaries delineated in neighboring Nissl-stained sections, and fluorescent labeling of the projections came nearly exclusively from injections in the ipsilateral hemisphere (Supplementary Figure 1). The densities of thalamic and cortical projections from PPC are shown for illustrative purposes, their densities were not quantified.

As seen in Figures 4A and B, tracer injections contained wholly within the cytoarchitectonic boundaries of PPC produced robust anterograde labeling in LP and Po, and farther anterior sections contained strong projections to LD (Supplementary Figure 2). In all cases, thalamic

projections were specific to associative nuclei with no staining in the immediately adjacent dorsal lateral geniculate nucleus (DLG), which receives projections from V1, nor in the ventral posterior medial nucleus (VPM), which receives projections from S1. Thus, the cortico-thalamic projections in the mouse appeared highly similar to those described in rats (Chandler *et al.*, 1992; Olsen & Witter, 2016). To visualize the position of the injection sites in PPC relative to other cortical areas, we examined flattened sections from the left hemisphere, which had similar triple injections at the same coordinates as the coronal sections. The myeloarchitecture in the flattened sections showed that our coordinates for PPC fell anterior and largely medial to V1, and tangential to the barrel fields of S1, in particular the δ barrel (Figure 4D).

To verify the projection targets of PPC, we next examined labeling resulting from triple-injections in coronal sections of the right hemisphere (Figure 5A, left), which showed prominent labeling in several cortical and sub-cortical regions. Anterior to PPC, this included projections targeting medial, ventral and ventrolateral orbitofrontal cortex (MO, VO, VLO; Figure 5B, left, MO not shown), with the most prominent labeling in superficial layers of VLO. The injections also produced strong labeling in cingulate (Cg) and secondary motor (M2) cortices, which appeared to follow a coarsely topographical distribution, with medial PPC projecting medially toward Cg, and lateral PPC projecting more laterally into M2 (Figure 5C-D, left). The projections from PPC to M2 were particularly strong posterior to bregma, though whether labeling was topographical at this level varied across animals (Supplementary Figure 3). We also noted that the projections to M2 corresponded well with prior descriptions of outputs from areas A and RL (Wang *et al.*, 2012). These connections, along with robust projections to primary somatosensory cortices (Figure 5E), and sub-cortical projections to the dorsal striatum and intermediate layers of the superior

colliculus (Supplementary Figure 2), are strongly consistent with the complement of connections described in rats (Kolb & Walkey, 1987; Chandler *et al.*, 1992; Wilber *et al.*, 2014a; Olsen & Witter, 2016). To determine whether these cortical outputs of PPC were reciprocal, we performed monosynaptic circuit tracing with rabies virus in a parallel series of mice (n = 4, Figure 5A, right) (Wickersham *et al.*, 2007), which showed unequivocally that PPC received monosynaptic inputs from each cortical area with anterograde labeling (Figure 5B-E, right).

Posteriorly, PPC projections were labeled in both superficial and deep layers of primary auditory cortex (Figure 6A), and in granular and agranular retrosplenial cortex (Figure 6B, top), which is consistent with observations in rats (Kolb & Walkey, 1987; Reep *et al.*, 1994; Wilber *et al.*, 2014a; Olsen & Witter, 2016) and could correspond to RSC projections from areas A and AM in mice (Wang *et al.*, 2012; Wilber *et al.*, 2014a). The densest projections from PPC were to extrastriate areas AM/V2M and AL/V2L (Figure 6B, middle and bottom), with AM/V2M showing a medial-to-lateral topography in line with the location of tracer injections in PPC, and AL/V2L in some cases showing a mirrored ordering (Figure 6B, bottom; Supplementary Figure 3, bottom). Although labeling from PPC was present farther posteriorly in areas PM and LM, it was weaker than in AM/V2M and AL/V2L, and did not appear topographical (not shown). As with cortical connections anterior to PPC, monosynaptic tracing with rabies virus confirmed these connections were reciprocal, originating from both deep and superficial layers in all upstream areas (Figure 6A and B, right).

DISCUSSION

In this study, we described laminar, cytoarchitectonic and chemoarchitectonic criteria for defining the mouse PPC and surrounding cortices which, to our knowledge, have not been established previously. By providing a characterization of PPC and its boundaries using intrinsic architectural features, this study differs from previous, large-scale investigations of the organization of mouse cortex based on functional connectivity and projection patterns (Lim *et al.*, 2012; Oh *et al.*, 2014; Zingg *et al.*, 2014). Importantly, we reconciled widely used but disparate nomenclatures that refer to PPC (Paxinos & Franklin, 2012) *versus* the extrastriate areas around it (Olavarria *et al.*, 1982; Olavarria & Montero, 1989; Montero, 1993; Wang & Burkhalter, 2007). We further confirmed our coordinates for PPC on the basis of projections to associative thalamic nuclei, which corresponded to thalamic projection patterns in rats (Kolb & Walkey 1987; Chandler et al. 1992; Bucci et al. 1999; Olsen & Witter 2016), mice (Harvey *et al.*, 2012) and several other mammalian species (Donoghue & Ebner, 1981; Olson & Lawler, 1987; Schmahmann & Pandya, 1990; Padberg & Krubitzer, 2006).

Considering the growing use of mice to study PPC and the networks with which it connects, advancing a straightforward cytoarchitectonic definition of the mouse PPC in relation to nearby areas is increasingly critical. The two major aims of this study were therefore (i) to provide a resource for identifying mouse PPC with anatomical criteria that are evident using ubiquitously available staining methods, such as a Nissl stain, and (ii) to define where PPC falls in relation to extrastriate areas around V1. The first evidence for such areas in mice came from studies of retinotopic processing in striate and extrastriate cortices (Wagor *et al.*, 1980), with subsequent investigations characterizing them based on anatomical projection patterns from V1 (Olavarria *et*

al., 1982; Olavarria & Montero, 1989). Later work established their connection strengths and retinotopic response properties systematically and at larger scales (Wang & Burkhalter, 2007; Andermann *et al.*, 2011; Marshel *et al.*, 2011; Garrett *et al.*, 2014), and their projections to other cortical areas were also mapped (Wang *et al.*, 2012). Since the dorsal cortical surface in rodents lacks gross anatomical landmarks, the pattern of responses in extrastriate areas have provided increasingly-used functional landmarks for locating higher visual (Garrett *et al.*, 2014) and associative regions in the posterior cortex (Olcese *et al.*, 2013; Driscoll *et al.*, 2017). However, functional mapping of this kind is not feasible in the absence of a broadly expressed calcium indicator or intrinsic optical imaging, and the location of these areas relative to PPC had not been defined explicitly until now.

By characterizing the architectural boundaries of PPC and cross-referencing them with projections from V1, we established that the anterior pole of PPC does not overlap with any extrastriate areas, whereas the posterior sectors of PPC overlap with areas A and AM (see Figure 7 for summary). The most lateral and posterior extent of PPC, area PtP (Paxinos & Franklin, 2012), overlapped partly with anterior area RL. These areas are referred to as "extrastriate", implying a primacy of visual processing (Wang & Burkhalter, 2007; Andermann *et al.*, 2011; Marshel *et al.*, 2011; Garrett *et al.*, 2014), though they overlap considerably with PPC, which has cognitive (Harvey *et al.*, 2012; Morcos & Harvey, 2016; Hwang *et al.*, 2017; Akrami *et al.*, 2018), navigational (Nitz, 2006; 2012), and movement-related (McNaughton *et al.*, 1994; Whitlock *et al.*, 2012) functions that can be expressed independently of visual input. For example, tetrode recordings in unrestrained rats targeting the posterior extent of PPC—appearing to coincide with area AM—showed widespread tuning to self-motion and angular head velocity in addition to visual

landmarks (Chen *et al.*, 1988; Chen *et al.*, 1994). Subsequent work spanning similar cortical territory also reported robust coding of self-motion and landmark positions in egocentric coordinates (Wilber *et al.*, 2014b; Wilber *et al.*, 2017), again indicating roles in behavior beyond purely visual processing, though visual signals or optic flow could contribute to such representations. The exact functions of PPC and surrounding extrastriate areas therefore merit further, systematic investigation outside of passive perceptual tasks, with substantial information likely to be gained from active or freely behaving animals.

Nevertheless, considerable portions of mouse PPC indeed receive input from V1, and its additional connections with auditory and somatosensory areas (Zingg *et al.*, 2014) are fully consistent with a role in multisensory processing (Olcese *et al.*, 2013; Raposo *et al.*, 2014). The parietal connections with frontal cortex likely support a role in elaborating movement, whereas connections with retrosplenial cortex and the dorsal presubiculum (Zingg *et al.*, 2014; Olsen *et al.*, 2017) likely contribute to navigation (Whitlock *et al.*, 2008; Save & Poucet, 2009) and, possibly, transformations from first-person to third-person reference frames (Byrne *et al.*, 2007; Alexander & Nitz, 2015). The general topological relationship between PPC and these extrinsic systems has been described to various extents across species, including rats (Kolb & Walkey, 1987), cats (Olson & Lawler, 1987), ferrets (Manger *et al.*, 2002), galagos (Stepniewska *et al.*, 2016), shrews (Remple *et al.*, 2006), new world (Gharbawie *et al.*, 2011) and old world monkeys (Cavada & Goldman-Rakic, 1989), and humans (Kaas & Stepniewska, 2016). Assuming that hodology is indicative of information flow, the connections of PPC would enable it to support potentially similar cognitive and behavioral functions in different species (Kaas, 1995; Krubitzer, 1995; Raposo *et al.*, 2012; Brunton *et al.*, 2013; Whitlock, 2014; Goldring & Krubbitzer, 2017; Whitlock, 2017), though the

relative weight of sensory inputs, for example, could vary according to evolutionary niches. The size and differentiation of PPC also differs substantially across species; in humans it consists of four distinct Brodmann areas 5, 7, 39, and 40 (Brodmann, 1909), while in macaques it includes areas 5 and 7, and in rats only an area 7 has been well described (Krieg, 1946; Olsen *et al*., 2016). Since the vast majority of recording studies in PPC have been in primates, and macaques in particular, the true degree of functional homology across species requires further recordings particularly in rodents, and with a detailed consideration of the animals' sensory processing and behavior.

As for mice, it remains to be mapped more fully where inputs from associative, motor, and sensory areas are integrated synaptically within PPC, and whether graded topographies exists for different sensory modalities, as shown for visual and vibrissal afferents in area RL (Olcese *et al.*, 2013). While the present study focused on characterizing PPC relative to extrastriate projections, comparable mapping could likely be performed in the context of somatosensory, auditory or motor inputs.

ACKNOWLEDGEMENTS

This work was supported by an ERC starting grant (agreement N^{o} 335328) to J.R.W., a Research Council of Norway grant to J.R.W. (agreement N^{o} 239963)**,** the Centre of Excellence scheme of the Research Council of Norway (Centre for Neural Computation, grant N^{o} 223262) and the National Infrastructure scheme of the Research Council of Norway – NORBRAIN, grant N^{o} 197467. We thank M. Carandini for helpful comments on the manuscript; G. M. Olsen for technical assistance, aiding with annotation and helpful discussions on comparative labeling in rats and mice; A. Burkhalter for generously sharing the flat map protocol; R.R. Nair and C. Kentros for generously sharing TVA and rabies viruses; H. Kleven and H. Waade for technical and IT assistance; members of the Whitlock lab for helpful discussions.

COMPETING INTERESTS

The authors declare no competing financial interests.

AUTHOR CONTRIBUTIONS

JRW and MPW conceived of and designed the study. KH performed all surgeries and histology. KH and MG analyzed the data. JRW and KH drafted the manuscript with input from MPW and MG.

DATA ACCESSIBILITY

Scans and confocal images of tissue used in this study can be made available upon request.

ORCID

Jonathan R. Whitlock: https://orcid.org/0000-0003-2642-8737

Menno P. Witter: https://orcid.org/0000-0003-0285-1637

ABBREVIATIONS

Cortical areas

Au	Auditory cortex
Cg	Cingulate cortex
EC	Entorhinal cortex
lPPC	Lateral posterior parietal cortex
M1	Primary motor cortex
M2	Secondary motor cortex
MO	Medial orbitofrontal cortex
mPPC	Medial posterior parietal cortex
POR	Postrhinal cortex
PPC	Posterior parietal cortex
PtP	Posterior part of parietal cortex
RSA	Agranular retrosplenial cortex
RSC	Retrosplenial cortex
RSG	Granular retrosplenial cortex
S1	Primary somatosensory cortex
S1B	Barrel fields of primary somatosensory cortex

Te	Temporal association cortex
V1	Primary visual cortex
V2L	Lateral secondary visual cortex
V2M	Medial secondary visual cortex
VLO	Ventrolateral orbitofrontal cortex
VO	Ventral orbitofrontal cortex

Extrastriate areas

A	Anterior area
AL	Anterolateral area
AM	Anteromedial area
LI	Laterointermediate area
LM	Lateromedial area
MM	Mediomedial area
P	Posterior area
PM	Posteriomedial area
RL	Rostrolateral area

Subcortical areas

DLG	Dorsal lateral geniculate nucleus
LD	Laterodorsal nucleus
LP	Lateral posterior nucleus
LPlr	Lateral posterior nucleus, anterolateral part
LPmr	Lateral posterior nucleus, anteromedial part
Po	Posterior thalamic nuclear group
SC	Superior colliculus
VPM	Ventral posterior nucleus, medial part

Visualized protein

M2AChR	Muscarinic acetylcholine receptor type 2
PV	Parvalbumin

REFERENCES

Akrami, A., Kopec, C.D., Diamond, M.E. & Brody, C.D. (2018) Posterior parietal cortex represents sensory history and mediates its effects on behaviour. *Nature*, **554**, 368-372.

Alexander, A.S. & Nitz, D.A. (2015) Retrosplenial cortex maps the conjunction of internal and external spaces. *Nature Neuroscience*, **18**, 1143-1151.

Andermann, M.L., Kerlin, A.M., Roumis, D.K., Glickfeld, L.L. & Reid, R.C. (2011) Functional specialization of mouse higher visual cortical areas. *Neuron*, **72**, 1025-1039.

Brodmann, K. (1909) *Vergleichende Lokalisationslehre der Grosshirnrinde in ihren Prinzipien dargestellt auf Grund des Zellenbauers.* Verlag von Johann Ambrosius Barth, Leipzig.

Brunton, B.W., Botvinick, M.M. & Brody, C.D. (2013) Rats and humans can optimally accumulate evidence for decision-making. *Science*, **340**, 95-98.

Bucci, D.J., Conley, M. & Gallagher, M. (1999) Thalamic and basal forebrain cholinergic connections of the rat posterior parietal cortex. *Neuroreport*, **10**, 941-945.

Byrne, P., Becker, S. & Burgess, N. (2007) Remembering the past and imagining the future: a neural model of spatial memory and imagery. *Psychological Review*, **114**, 340-375.

Cappe, C., Morel, A. & Rouiller, E.M. (2007) Thalamocortical and the dual pattern of corticothalamic projections of the posterior parietal cortex in macaque monkeys. *Neuroscience*, **146**, 1371-1387.

Cavada, C. & Goldman-Rakic, P.S. (1989) Posterior parietal cortex in rhesus monkey: I. Parcellation of areas based on distinctive limbic and sensory corticocortical connections. *The Journal of Comparative Neurology*, **287**, 393-421.

Chandler, H.C., King, V., Corwin, J.V. & Reep, R.L. (1992) Thalamocortical connections of rat posterior parietal cortex. *Neuroscience Letters*, **31**, 237-242.

Chen, L.L., Lin, L.H., Barnes, C.A. & McNaughton, B.L. (1994) Head-direction cells in the rat posterior cortex. ii. Contributions of visual and ideothetic information to the directional firing. *Experimental brain research. Experimentelle Hirnforschung*, **101**, 24-34.

Chen, L.L. & McNaughton B.L. (1988) Spatially selective discharge of vision and movement modulated posterior parietal neurons in the rat. . Vol. 14, Soc. Neurosci. Abstracts. City. p. 818.

D'Souza, R.D., Meier, A.M., Bista, P., Wang, Q. & Burkhalter, A. (2016) Recruitment of inhibition and excitation across mouse visual cortex depends on the hierarchy of interconnecting areas. *Elife*, **5**.

Donoghue, J.P. & Ebner, F.F. (1981) The organization of thalamic projections to the parietal cortex of the Virginia opossum. *The Journal of Comparative Neurology*, **198**, 365-388.

Driscoll, L.N., Pettit, N.L., Minderer, M., Chettih, S.N. & Harvey, C.D. (2017) Dynamic Reorganization of Neuronal Activity Patterns in Parietal Cortex. *Cell*, **170**, 986-999.

Garrett, M.E., Nauhaus, I., Marshel, J.H. & Callaway, E.M. (2014) Topography and areal organization of mouse visual cortex. *The Journal of Neuroscience*, **34**, 12587-12600.

Gharbawie, O.A., Stepniewska, I. & Kaas, J.H. (2011) Cortical connections of functional zones in posterior parietal cortex and frontal cortex motor regions in new world monkeys. *Cerebral Cortex*, **21**, 1981-2002.

Goard, M.J., Pho, G.N., Woodson, J. & Sur, M. (2016) Distinct roles of visual, parietal, and frontal motor cortices in memory-guided sensorimotor decisions. *Elife*, **5**.

Goldring, A., Krubitzer, L. (2017) Evolution of parietal cortex in mammals: From manipulation to tool use. In Krubitzer, L., Kaas, J.H. (eds) *The Evolution of Nervous Systems*. Elsevier, London, pp. 259-286.

Harvey, C.D., Coen, P. & Tank, D.W. (2012) Choice-specific sequences in parietal cortex during a virtual-navigation decision task. *Nature*, **484**, 62-68.

Hwang, E.J., Dahlen, J.E., Mukundan, M. & Komiyama, T. (2017) History-based action selection bias in posterior parietal cortex. *Nature Communications*, **8**, 1242.

Kaas, J.H. (1995) The evolution of isocortex. *Brain, Behavior and Evolution*, **46**, 187-196.

Kaas, J.H. & Stepniewska, I. (2016) Evolution of posterior parietal cortex and parietal-frontal networks for specific actions in primates. *The Journal of Comparative Neurology*, **524**, 595-608.

Kolb, B. & Walkey, J. (1987) Behavioural and anatomical studies of the posterior parietal cortex in the rat. *Behavioural Brain Research*, **23**, 127-145.

Krieg, W.J.S. (1946) Connections of the cerebral cortex: I. The albino rat. B. Structure of the cortical areas. *Journal of Comparative Neurology*, **84**, 277-323.

Krubitzer, L. (1995) The organization of neocortex in mammals: are species differences really so different? *Trends in Neuroscience*, **18**, 408-417.

Lim, D.H., Mohajerani, M.H., Ledue, J., Boyd, J., Chen, S. & Murphy, T.H. (2012) In vivo Large-Scale Cortical Mapping Using Channelrhodopsin-2 Stimulation in Transgenic Mice Reveals Asymmetric and Reciprocal Relationships between Cortical Areas. *Frontiers in Neural Circuits*, **6**, 11.

Manger, P.R., Masiello, I. & Innocenti, G.M. (2002) Areal organization of the posterior parietal cortex of the ferret (Mustela putorius). *Cerebral Cortex*, **12**, 1280-1297.

Marshel, J.H., Garrett, M.E., Nauhaus, I. & Callaway, E.M. (2011) Functional specialization of seven mouse visual cortical areas. *Neuron*, **72**, 1040-1054.

McDaniel, W.F., McDaniel, S.E. & Thomas, R.K. (1978) Thalamocortical projections to the temporal and parietal association cortices in the rat. *Neuroscience Letters*, **7**, 121-125.

McNaughton, B.L., Mizumori, S.J., Barnes, C.A., Leonard, B.J., Marquis, M. & Green, E.J. (1994) Cortical representation of motion during unrestrained spatial navigation in the rat. *Cerebral Cortex*, **4**, 27-39.

Montero, V.M. (1993) Retinotopy of cortical connections between the striate cortex and extrastriate visual areas in the rat. *Experimental Brain Research*, **94**, 1-15.

Morcos, A.S. & Harvey, C.D. (2016) History-dependent variability in population dynamics during evidence accumulation in cortex. *Nature Neuroscience*, **19**, 1672-1681.

Nitz, D.A. (2006) Tracking route progression in the posterior parietal cortex. *Neuron*, **49**, 747-756.

Nitz, D.A. (2012) Spaces within spaces: rat parietal cortex neurons register position across three reference frames. *Nature Neuroscience*, **15**, 1365-1367.

Oh, S.W., Harris, J.A., Ng, L., Winslow, B., Cain, N., Mihalas, S., Wang, Q., Lau, C., Kuan, L., Henry, A.M., Mortrud, M.T., Ouellette, B., Nguyen, T.N., Sorensen, S.A., Slaughterbeck, C.R., Wakeman, W., Li, Y., Feng, D., Ho, A., Nicholas, E., Hirokawa, K.E., Bohn, P., Joines, K.M., Peng, H., Hawrylycz, M.J., Phillips, J.W., Hohmann, J.G., Wohnoutka, P., Gerfen, C.R., Koch, C., Bernard, A., Dang, C., Jones, A.R. & Zeng, H. (2014) A mesoscale connectome of the mouse brain. *Nature*, **508**, 207-214.

Olavarria, J., Mignano, L.R. & Van Sluyters, R.C. (1982) Pattern of extrastriate visual areas connecting reciprocally with striate cortex in the mouse. *Experimental Neurology*, **78**, 775-779.

Olavarria, J. & Montero, V.M. (1989) Organization of visual cortex in the mouse revealed by correlating callosal and striate-extrastriate connections. *Visual Neuroscience*, **3**, 59-69.

Olcese, U., Iurilli, G. & Medini, P. (2013) Cellular and synaptic architecture of multisensory integration in the mouse neocortex. *Neuron*, **79**, 579-593.

Olsen, G.M., Ohara, S., Iijima, T. & Witter, M.P. (2017) Parahippocampal and retrosplenial connections of rat posterior parietal cortex. *Hippocampus*, **27**, 335-358.

Olsen, G.M. & Witter, M.P. (2016) Posterior parietal cortex of the rat: Architectural delineation and thalamic differentiation. *The Journal of Comparative Neurology*, **524**, 3774-3809.

Olson, C.R. & Lawler, K. (1987) Cortical and subcortical afferent connections of a posterior division of feline area 7 (area 7p). *The Journal of Comparative Neurology*, **259**, 13-30.

Padberg, J. & Krubitzer, L. (2006) Thalamocortical connections of anterior and posterior parietal cortical areas in New World titi monkeys. *The Journal of Comparative Neurology*, **497**, 416-435.

Paxinos, G. & Franklin, K. (2012) *Paxino's and Franklin's the Mouse Brain in Stereotaxic Coordinates*. Academic Press.

Paxinos, G. & Watson, C. (2013) *The Rat Brain in Stereotaxic Coordinates*. Academic Press.

Raposo, D., Kaufman, M.T. & Churchland, A.K. (2014) A category-free neural population supports evolving demands during decision-making. *Nature Neuroscience*, **17**, 1784-1792.

Raposo, D., Sheppard, J.P., Schrater, P.R. & Churchland, A.K. (2012) Multisensory decision-making in rats and humans. *The Journal of Neuroscience*, **32**, 3726-3735.

Reep, R.L., Chandler, H.C., King, V. & Corwin, J.V. (1994) Rat posterior parietal cortex: topography of corticocortical and thalamic connections. *Experimental Brain Research*, **100**, 67-84.

Remple, M.S., Reed, J.L., Stepniewska, I. & Kaas, J.H. (2006) Organization of frontoparietal cortex in the tree shrew (Tupaia belangeri). I. Architecture, microelectrode maps, and corticospinal connections. *The Journal of Comparative Neurology*, **497**, 133-154.

Save, E. & Poucet, B. (2009) Role of the parietal cortex in long-term representation of spatial information in the rat. *Neurobioligy of Learning and Memory*, **91**, 172-178.

Schmahmann, J.D. & Pandya, D.N. (1990) Anatomical investigation of projections from thalamus to posterior parietal cortex in the rhesus monkey: a WGA-HRP and fluorescent tracer study. *The Journal of Comparative Neurology*, **295**, 299-326.

Stepniewska, I., Cerkevich, C.M. & Kaas, J.H. (2016) Cortical Connections of the Caudal Portion of Posterior Parietal Cortex in Prosimian Galagos. *Cerebral Cortex*, **26**, 2753-2777.

Wang, Q. & Burkhalter, A. (2007) Area map of mouse visual cortex. *The Journal of Comparative Neurology*, **502**, 339-357.

Wang, Q., Sporns, O. & Burkhalter, A. (2012) Network analysis of corticocortical connections reveals ventral and dorsal processing streams in mouse visual cortex. *The Journal of Neuroscience*, **32**, 4386-4399.

Wagor, E., Mangini, N.J. & Pearlman, A.L. (1980) Retinotopic organization of striate and extrastriate visual cortex in the mouse. *The Journal of Comparative Neurology*, **193**, 187-202.

Whitlock, J.R., Pfuhl, G., Dagslott, N., Moser, M.B. & Moser, E.I. (2012) Functional split between parietal and entorhinal cortices in the rat. *Neuron*, **73**, 789-802.

Whitlock, J.R., Sutherland, R.J., Witter, M.P., Moser, M.B. & Moser, E.I. (2008) Navigating from hippocampus to parietal cortex. *Proc Natl Acad Sci U S A*, **105**, 14755-14762.

Whitlock, J.R. (2014) Navigating actions through the rodent parietal cortex. *Frontiers in Human Neuroscience*, **8**, 293.

Whitlock, J.R. (2017) Posterior parietal cortex. *Current Biology*, **27**, R691-R695.

Wickersham, I.R., Lyon, D.C., Barnard, R.J., Mori, T., Finke, S., Conzelmann, K.K., Young, J.A. & Callaway, E.M. (2007) Monosynaptic restriction of transsynaptic tracing from single, genetically targeted neurons. *Neuron*, **53**, 639-647.

Wilber, A.A., Clark, B.J., Demecha, A.J., Mesina, L., Vos, J.M. & McNaughton, B.L. (2014a) Cortical connectivity maps reveal anatomically distinct areas in the parietal cortex of the rat. *Frontiers in Neural Circuits*, **8**, 146.

Wilber, A.A., Clark, B.J., Forster, T.C., Tatsuno, M. & McNaughton, B.L. (2014b) Interaction of egocentric and world-centered reference frames in the rat posterior parietal cortex. *The Journal of Neuroscience*, **34**, 5431-5446.

Wilber, A.A., Skelin, I., Wu, W. & McNaughton, B.L. (2017) Laminar Organization of Encoding and Memory Reactivation in the Parietal Cortex. *Neuron*, **95**, 1406-1419 e1405.

Wise, S.P., Boussaoud, D., Johnson, P.B. & Caminiti, R. (1997) Premotor and parietal cortex: corticocortical connectivity and combinatorial computations. *Annual Review of Neuroscience*, **20**, 25-42.

Zilles, K. (1985) *The cortex of the rat: a stereotaxic atlas.* Springer-Verlag Berlin Heidelberg.

Zingg, B., Hintiryan, H., Gou, L., Song, M.Y., Bay, M., Bienkowski, M.S., Foster, N.N., Yamashita, S., Bowman, I., Toga, A.W. & Dong, H.W. (2014) Neural networks of the mouse neocortex. *Cell*, **156**, 1096-1111.

FIGURE LEGENDS

Figure 1. Delineation of posterior parietal cortex and surrounding areas. Coronal sections of Nissl- (left), parvalbumin- (middle) and M2AChR-stained (right) tissue from a single mouse are shown in 40µm sections in three interleaved series. Approximate bregma levels, based on Paxinos & Franklin (2012), are indicated at the far left, along with a hemispheric overview of where the sections on the right were taken from. The nomenclature is also adapted from Paxinos & Franklin (2012); see list for abbreviations. Left scale bar = 1mm, right scale bar = 500µm.

Figure 2. Projections from V1 viewed in flattened (left) and coronal (right) sections. (**A**) Left hemisphere: Section through layer IV of flattened cortex showing triple injections of anterograde tracers in V1 and the resulting projections to extrastriate areas. Insert: dark-field image from an unprocessed section for overview. Nomenclature for the visual projection fields is based on Montero (1993), and cortical field boundaries were established within-hemisphere. The outlines of V1 and barrels of S1 were drawn from M2AChR staining and myeloarchitecture from the dark-field image (see insert, top left). To avoid signal saturation from the injection sites, a shorter exposure time was used for injection sites than for projections as shown in the image (Methods). (**B**) Right hemisphere: triple injections of anterograde tracers in V1 (section 8, at bottom) as in **A**, visualized in coronal sections, as well as the resulting projections to extrastriate areas. Anterior-posterior levels of the coronal section are indicated by corresponding numbers (1 through 8) in **A**, the locations of which are estimates based on the similarity of labeling patterns and AP levels. Projections from V1 to areas LM, LI and AL were topographically organized, whereas labeling was

intermingled in other sub-fields. (**C**) Magnified view of labeling from highlighted areas in coronal sections in **B**. The figure is for illustration purposes. See list for abbreviations. Scale bars in **A** and **B** = 500µm, in **C** = 200µm.

Figure 3. Co-registration of extrastriate areas with PPC and surrounding cortices. (**A**) Tissue from the same triple injections in V1 as in Figure 2 are shown, along with Nissl- and M2-stained sections from the same brain. Each panel consists of three immediately adjacent sections, with the series starting in PPC and proceeding posteriorly (AP coordinates estimated using Paxinos & Franklin, 2012). The nomenclature for extrastriate areas is based on Montero (1993) and Wang & Burkhalter (2007), and the cyto- and chemoarchitectonic labels are adapted from Paxinos & Franklin (2012). (**B**) A comparison of the three sections shows that mPPC at this level does not overlap with any extrastriate areas, whereas lPPC overlaps with area A. The enlarged inset above shows the fluorescent processes of area A / lPPC (nomenclatures juxtaposed at bottom left). (**C-G**) Similar comparisons from tissue sections spanning approximately -2 to -4mm AP. Scale bar at bottom right of **G** = 500µm; insert = 50µm.

Figure 4. Validation of coordinates for PPC using thalamic labeling. (**A**) A Nissl-stained section from the right hemisphere showing triple injections of dextran amine tracers within cytoarchitectonic boundaries of PPC in that hemisphere, with the underlying thalamic nuclei delineated (inset). (**B**) Fluorescent image of the same section, showing fluorescent anterograde labeling in the associative thalamic nuclei LP and Po, with no staining in the DLG. (**C**) Overview of

flattened cortex showing triple anterograde tracer injections in V1 in a different mouse, along with S1B, S1, RSC and an estimation of where PPC should fall. (**D**) Triple anterograde injections at the same coordinates as A and B, in the left hemisphere of the same animal, viewed in a flat map with the area estimated as PPC directly lateral to the δ barrel field. In both (**C**) and (**D**), cortical area boundaries are drawn based on within-hemisphere myeloarchitecture, and exposure times and saturation levels for the images were optimized to highlight injections sites, not labeled projections. Scale bars at bottom right of **A-D** = 500μm; insert = 100μm.

Figure 5. Efferent and afferent cortical connections anterior to PPC. (**A**) (left) Coronal section showing triple anterograde tracer injections in PPC of the right hemisphere; (right) injection site of TVAG and rabies viruses in the right hemisphere of a different mouse. Cortical boundaries were drawn based on cytoarchitectural features in Nissl-stained sections adjacent to each section with anterograde or retrograde labeling, in correspondence with Paxinos & Franklin (2012). (**B**) (left) Drawing of the right hemisphere at +2.57mm from bregma, from which the middle and right panels were taken. (middle) Fluorescent images of PPC projections to VO and VLO, (right) retrograde rabies labeling (red) against Hoechst counterstaining (blue). (**C**) (left) Drawing of the right hemisphere at +0.49mm from bregma. (middle) Strong anterograde labeling in Cg and M2, showing a rough topographical correspondence with injection sites in PPC. (right) Rabies labeling indicated dense monosynaptic projections from dorsal Cg cortex and medial M2 to PPC. (**D**) (left) Same as above, toward the posterior extent of M2, (middle) fluorescent anterograde projections from medial and lateral PPC; (right) retrogradely labeled neurons in posterior M2 and Cg that project to PPC. (**E**) (left) Drawing of the right hemisphere at -1.31mm relative to bregma. (middle)

At this level, PPC has robust projections to S1, and (right) rabies labeling in S1 shows the connection is reciprocal. Scale bars in **B-E** = 500µm in left panels, 200µm in middle and right panels.

Figure 6. Efferent and afferent cortical connections posterior to PPC. Anterograde and retrograde labeling resulting from the same injections as in Figure 5; cortical boundaries were drawn based on adjacent Nissl-stained sections, in correspondence with Paxinos & Franklin (2012). (**A**) (left) Drawing of the right hemisphere at -2.03mm from bregma, from which the middle and right panels were taken. (middle) PPC projects to deep and superficial layers of auditory cortex (Au); (right) Au provides monosynaptic input back to PPC, as indicated by rabies tracing. (**B**) (left) Same as above, at -2.69mm relative to bregma. (middle) PPC projections were present in superficial and deep layers of RSC (top), but were stronger and clearly topographical in AM and AL (lower panels). (right) Deep and superficial RSC, as well as areas AM and AL provide monosynaptic input to PPC. Scale bar = 500µm in left panels, 200µm in middle and right panels.

Figure 7. Summary of the location, architectural characteristics and connectivity of mouse PPC. (left) Schematic of the dorsal cortical surface with boundaries outlined for major sensory, motor and associative regions. The seven extrastriate areas considered in this study are drawn around V1. Each of the PPC sub-areas, defined architectonically, are superimposed in color. The anterior pole of PPC does not overlap with any extrastriate areas while, more posteriorly, mPPC overlaps with the anterior portion of area AM, lPPC overlaps extensively with area A, and PtP overlaps with

the anterior pole of area RL. Laterally, the posterior row of S1 barrel fields are drawn with the delta barrel labeled. Dimensions are in millimeters and referenced to bregma (B). (right, top) Brief description of distinguishing laminar and cytoarchitectonic features for each PPC sub-area. (right, bottom) Summary of thalamic, cortical and sub-cortical connections of PPC described in the present study, including connections for LM and PM as described by Wang & Burkhalter (2012).

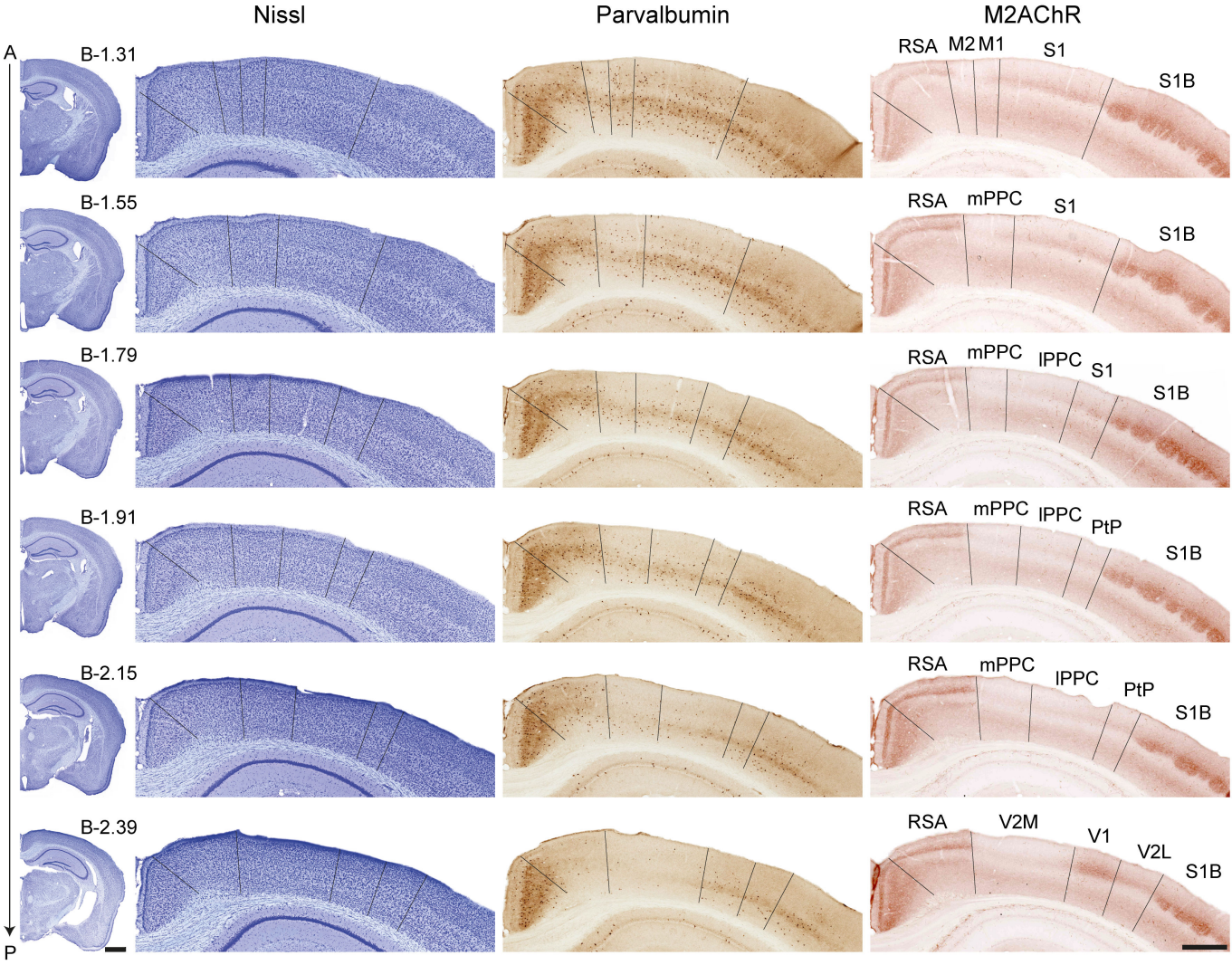
Nissl
Parvalbumin
M2AChR
A
P
B-1.31
B-1.55
B-1.79
B-1.91
B-2.15
B-2.39
RSA
M2
M1
S1
S1B
mPPC
lPPC
PtP
V2M
V1
V2L

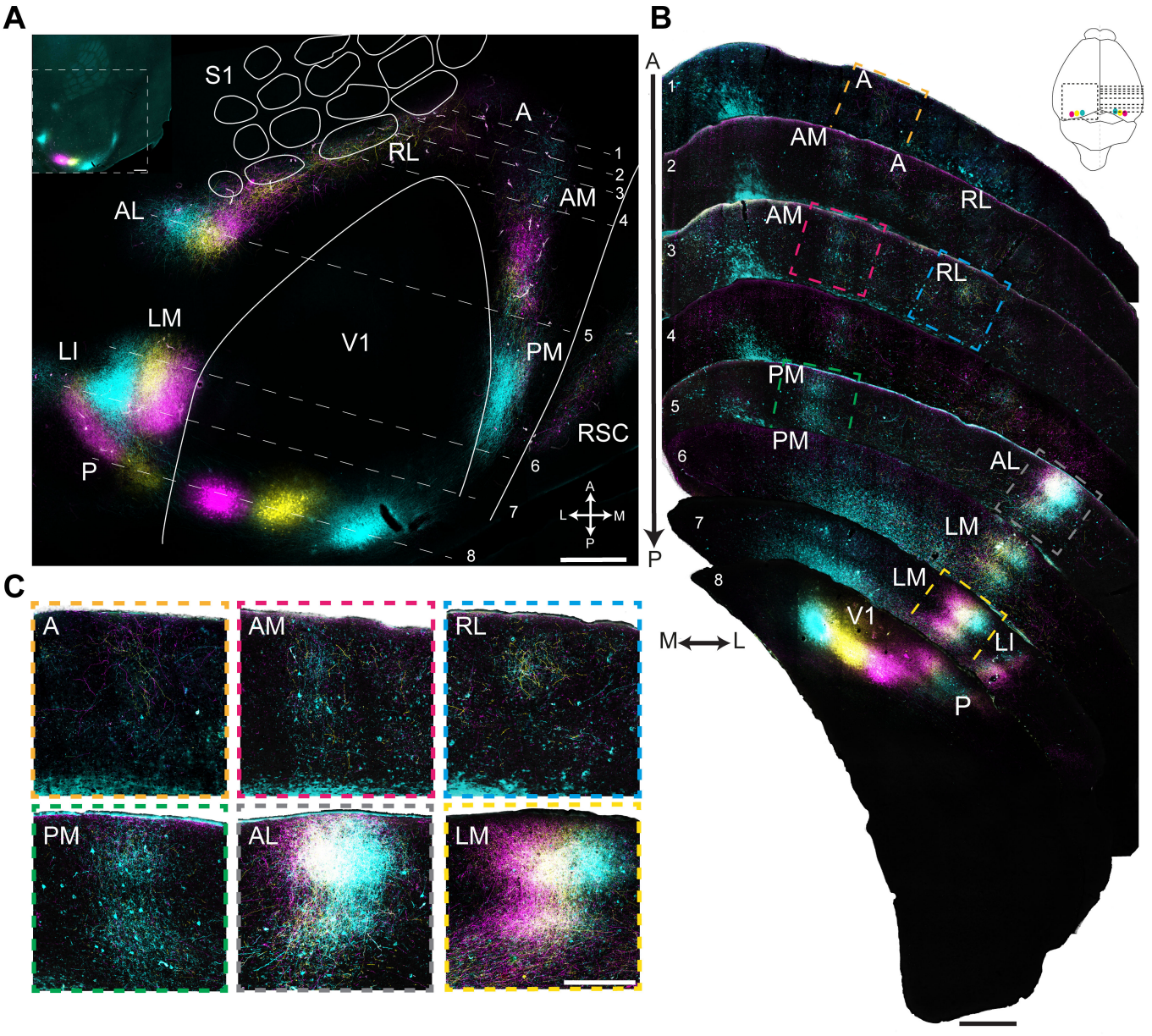
A
S1
A
RL
AM
AL
1
2
3
4
LM
LI
V1
PM
5
RSC
P
6
7
8
A
L
M
P
B
A
1
A
AM
A
2
RL
AM
3
RL
4
PM
5
PM
6
AL
LM
7
LM
8
V1
LI
M
L
P
C
A
AM
RL
PM
AL
LM

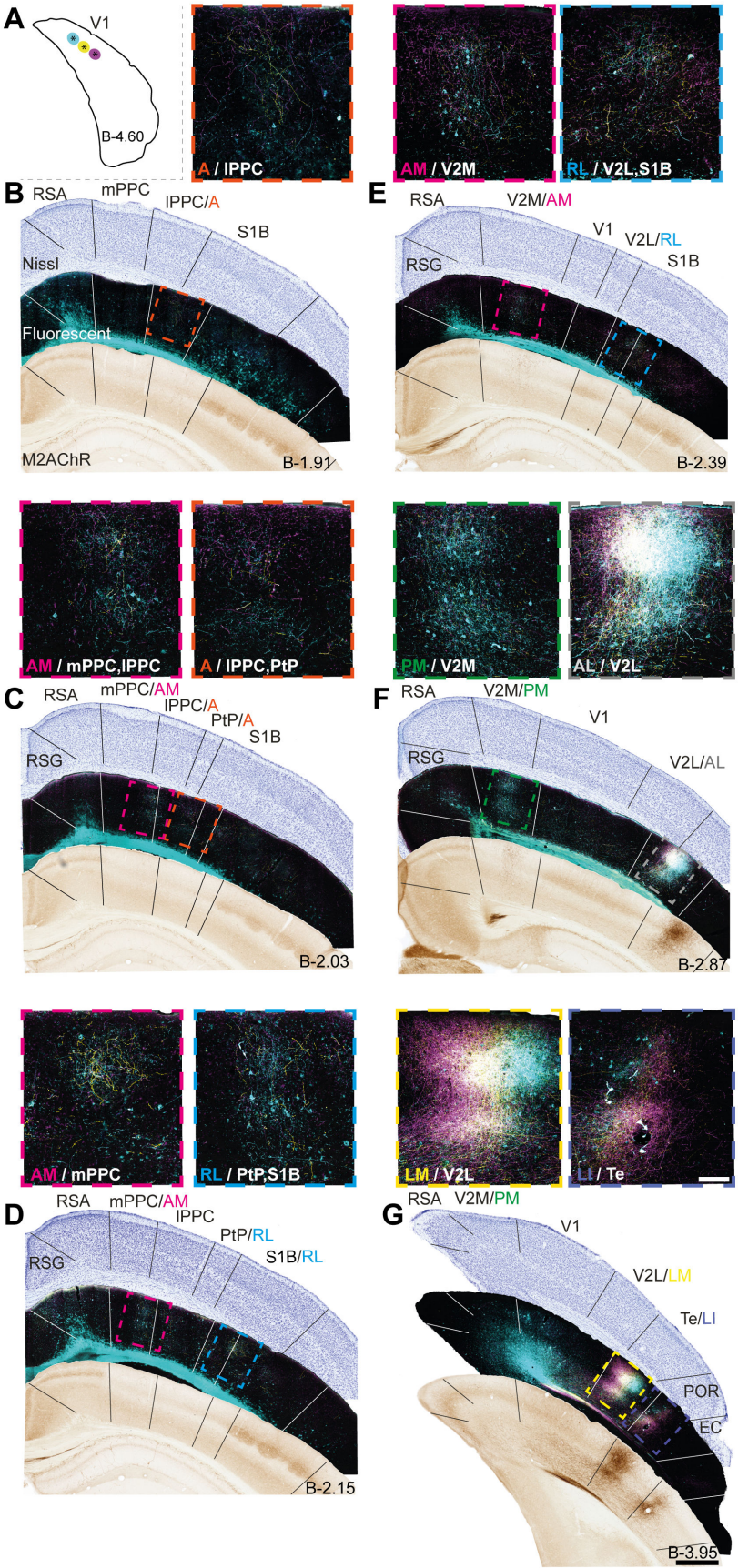
A
V1
B-4.60
A / lPPC
AM / V2M
RL / V2L,S1B
B
RSA
mPPC
lPPC/A
S1B
Nissl
Fluorescent
M2AChR
B-1.91
E
RSA
V2M/AM
V1
V2L/RL
S1B
RSG
B-2.39
AM / mPPC,lPPC
A / lPPC,PtP
PM / V2M
AL / V2L
C
RSA
mPPC/AM
lPPC/A
PtP/A
S1B
RSG
B-2.03
F
RSA
V2M/PM
V1
RSG
V2L/AL
B-2.87
AM / mPPC
RL / PtP,S1B
LM / V2L
LI / Te
D
RSA
mPPC/AM
lPPC
PtP/RL
S1B/RL
RSG
B-2.15
G
RSA
V2M/PM
V1
V2L/LM
Te/LI
POR
EC
B-3.95

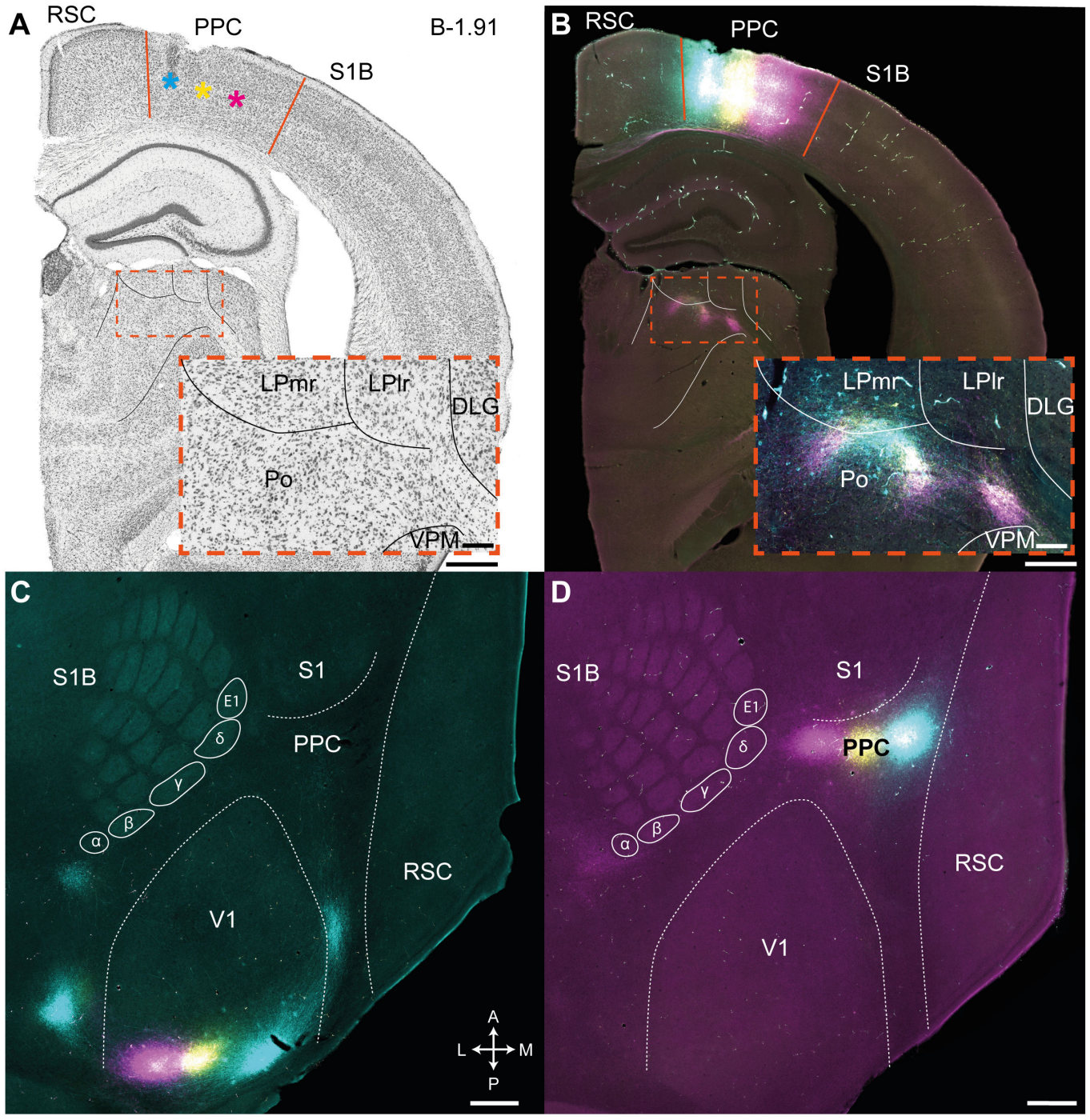
A
RSC
PPC
B-1.91
S1B
LPmr
LPlr
DLG
Po
VPM
B
RSC
PPC
S1B
LPmr
LPlr
DLG
Po
VPM
C
S1B
S1
E1
δ
γ
β
α
PPC
RSC
V1
A
L
M
P
D
S1B
S1
E1
δ
γ
β
α
PPC
RSC
V1

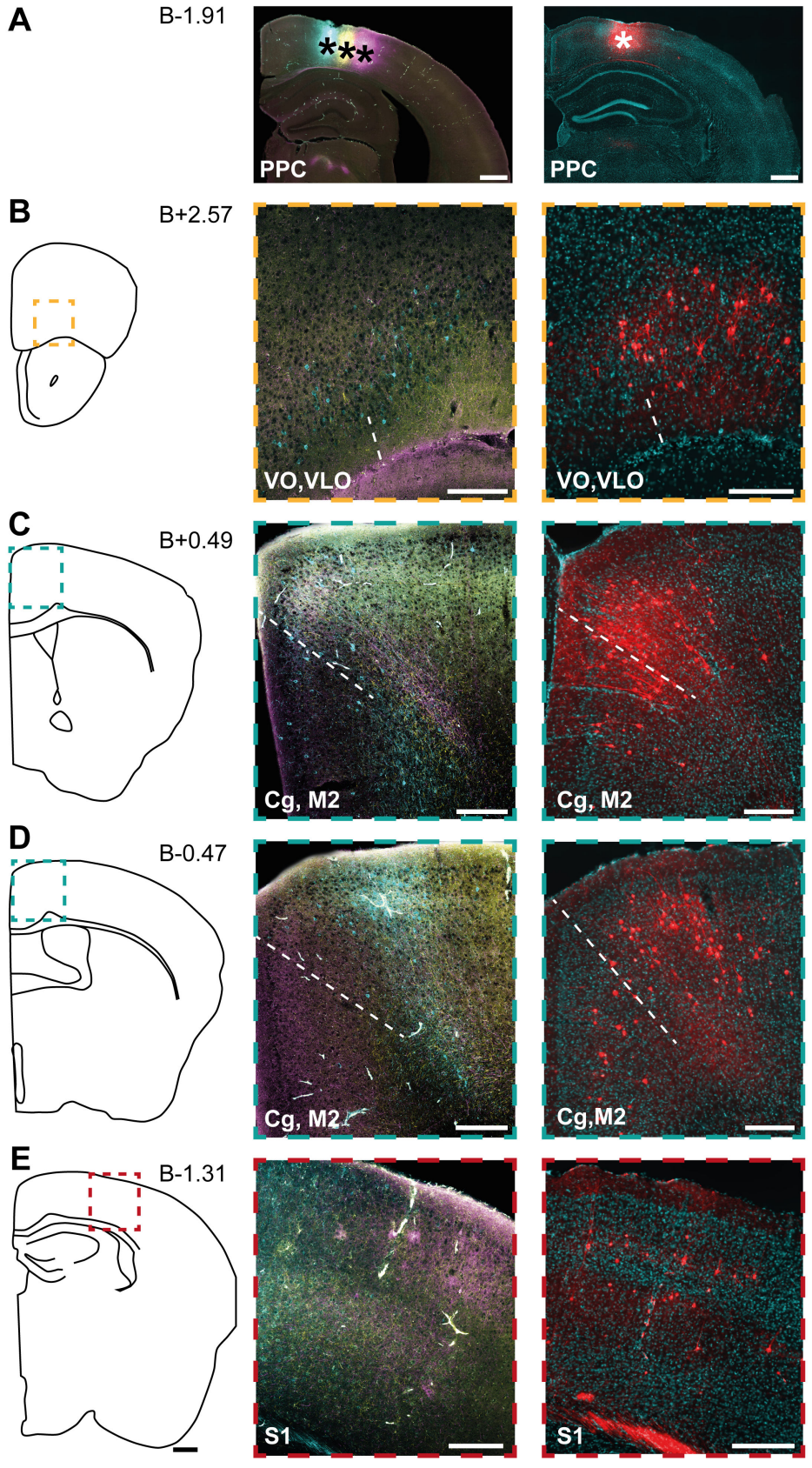
A
B-1.91
***
PPC
*
PPC
B
B+2.57
VO,VLO
VO,VLO
C
B+0.49
Cg, M2
Cg, M2
D
B-0.47
Cg, M2
Cg,M2
E
B-1.31
S1
S1

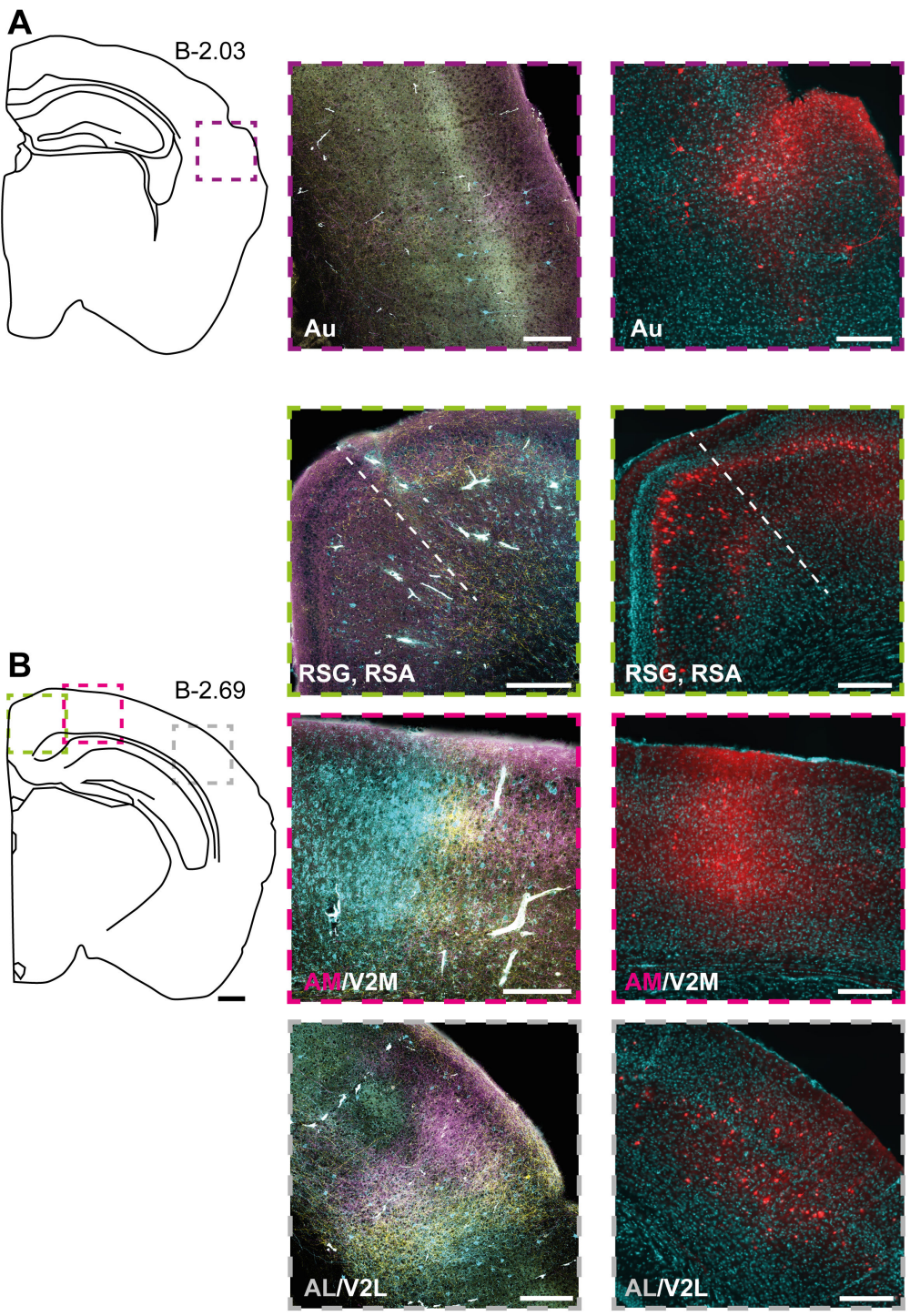
A
B-2.03
Au
Au
RSG, RSA
RSG, RSA
B
B-2.69
AM/V2M
AM/V2M
AL/V2L
AL/V2L

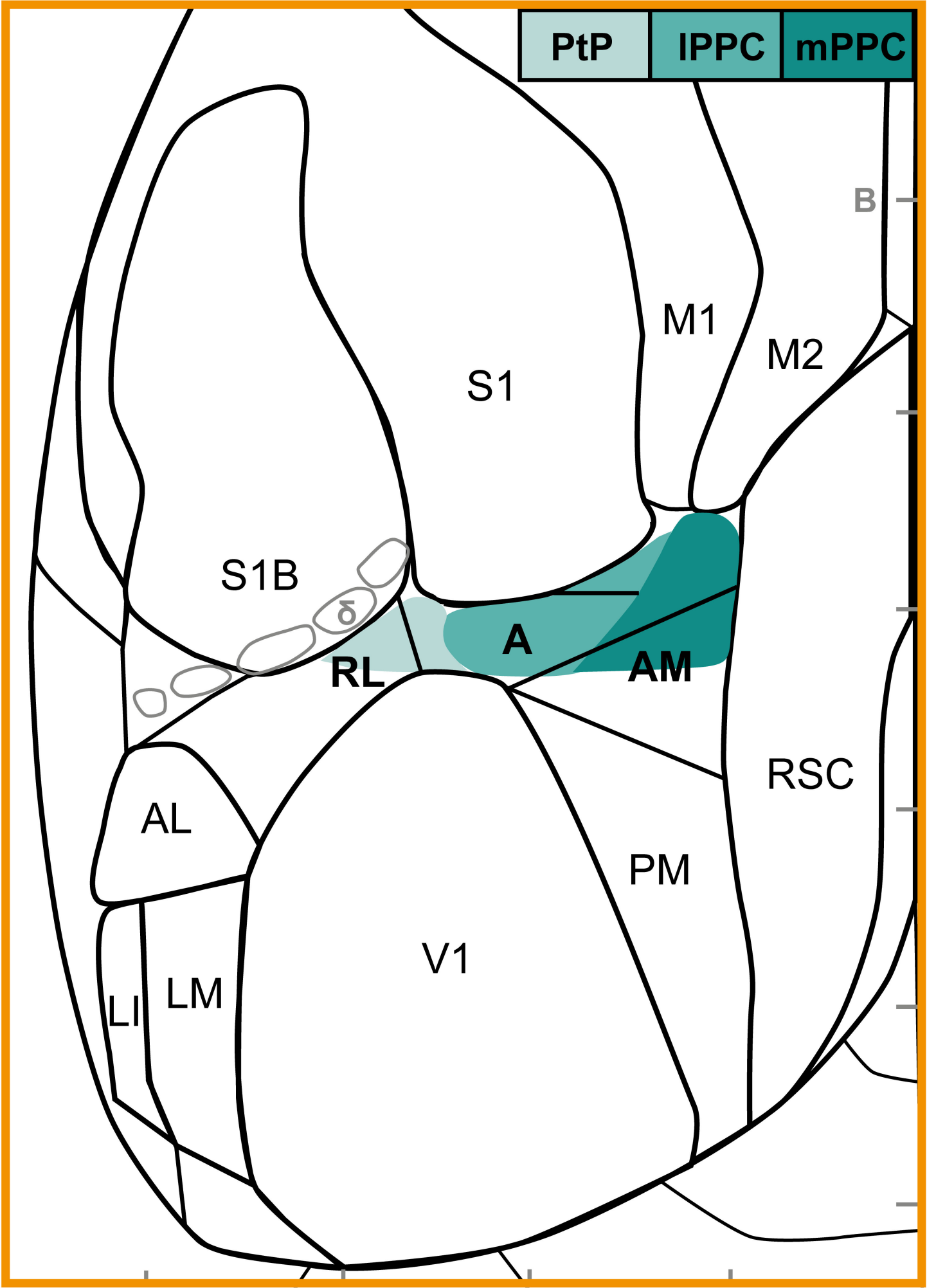
PtP
lPPC
mPPC
B
M1
M2
S1
S1B
δ
A
RL
AM
RSC
AL
PM
V1
LI
LM

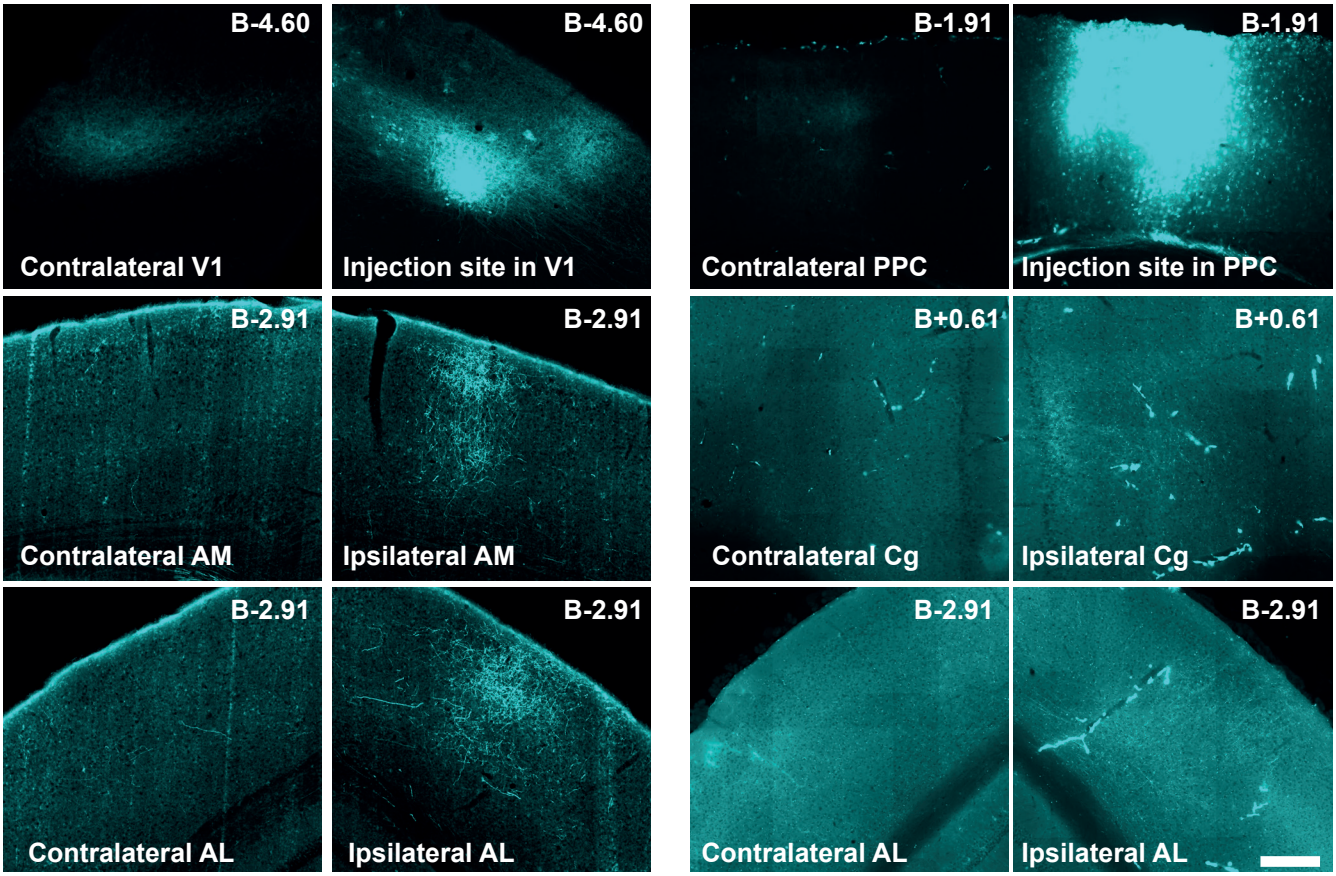

Supplementary Figure 1. Anterograde tracer labeling was primarily ipsilateral.
(Left top) A unilateral BDA tracer injection in V1 (brain 74749) and the resulting anterograde labeling in ipsi- and contralateral hemispheres. The injection produced contralateral labeling at the level of the injection site in V1 (top row), but little to no staining in contralateral areas AM (middle row) and AL (bottom row). Conversely, ipsilateral staining of projections was readily visible for both AM and AL. (Top right) A similar unilateral dextran 488 injection was made in PPC of a separate mouse (brain 72934), again showing labeling for ipsilateral, but not contralateral, projections to cingulate cortex (middle row) and area AL (bottom). For all images, each hemisphere is a crop out of the same section and set to the same brightness, and the color of the tracer is rendered in cyan for visualization purposes. Scalebar = 200μm.

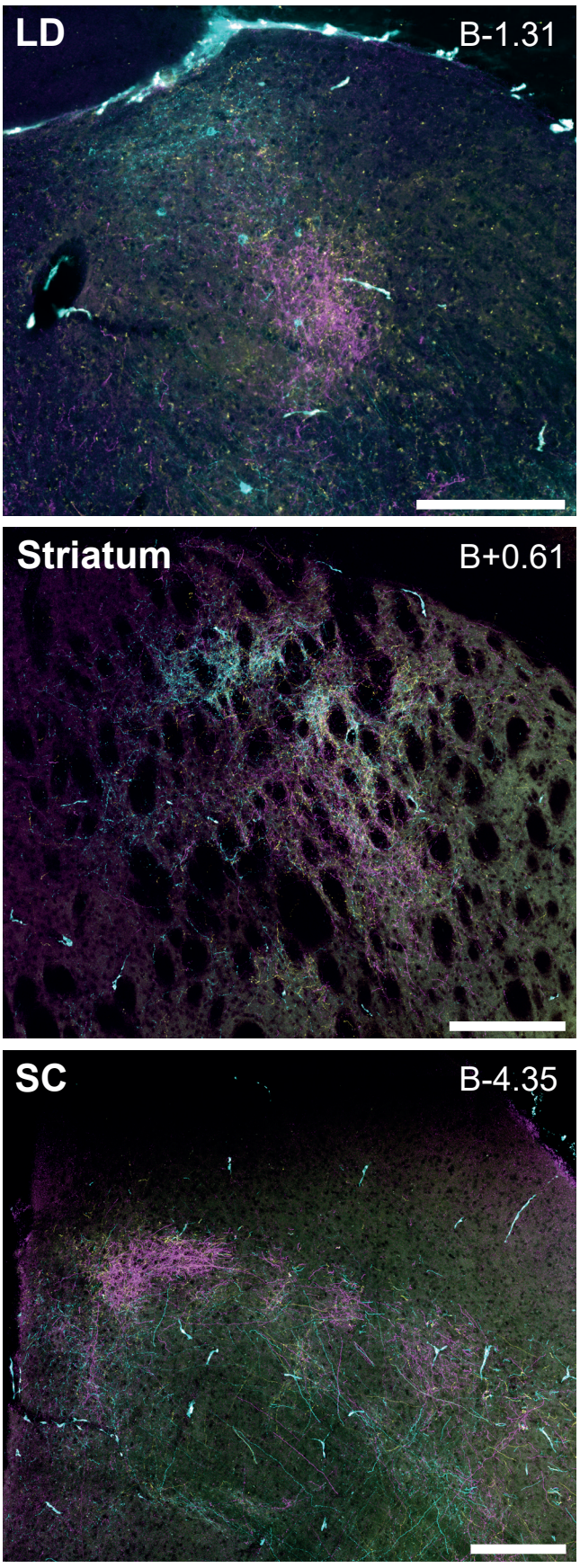

Supplementary Figure 2. Subcortical targets of PPC projections.
(top) Anterograde labeling in the lateral dorsal (LD) nucleus of the thalamus was readily apparent following triple anterograde tracer injections in PPC. This section is from the same brain as in Figures 4A and B, anterior to thalamic labeling in LP and Po. (middle) Projections to the dorsal striatum and (bottom) intermediate layers of the superior colliculus. Scale bars = 200μm.

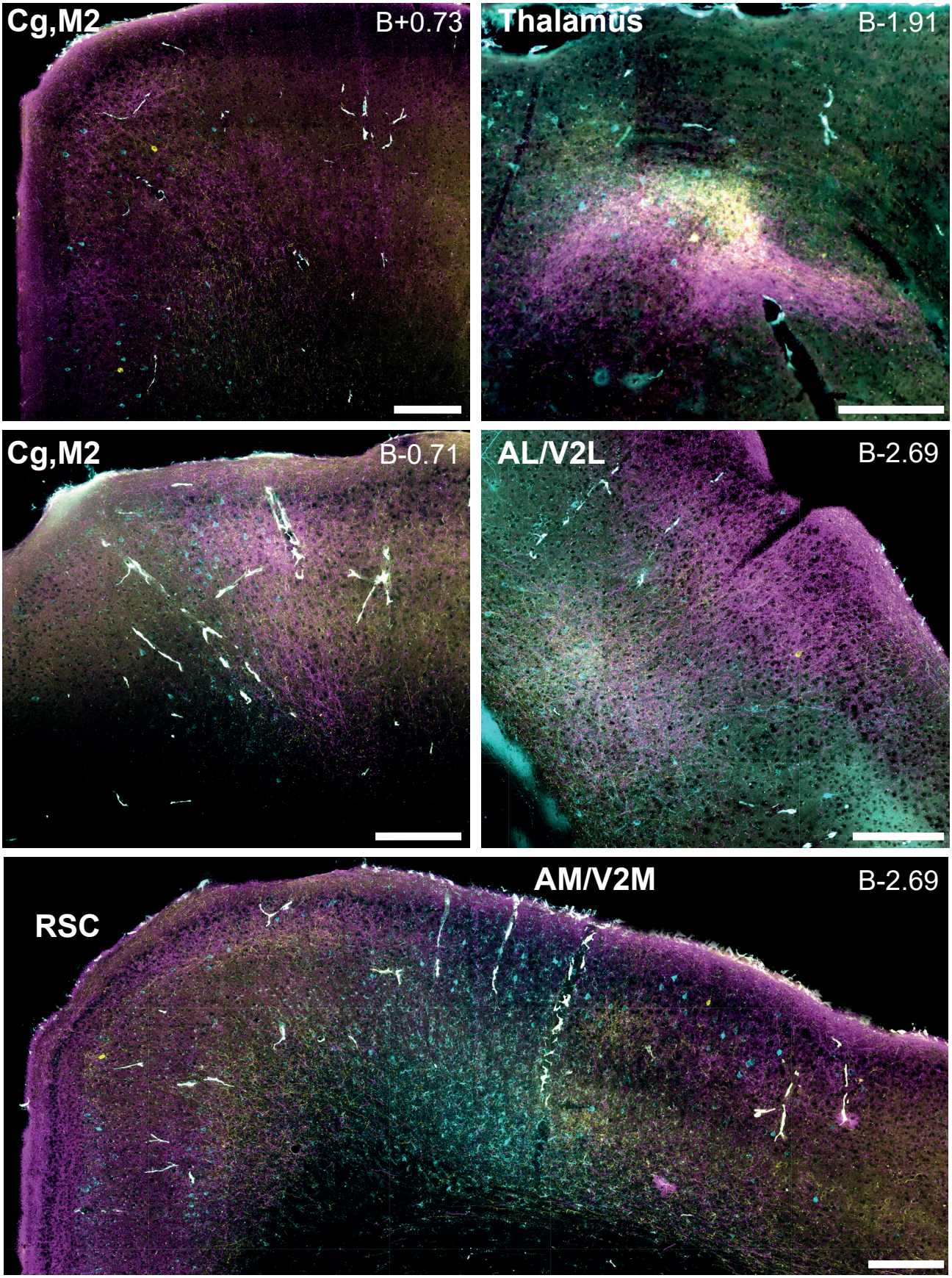

Supplementary Figure 3. Projections of PPC were consistent across mice.
Anterograde labeling following triple tracer injections in another mouse (74574) closely matched the patterns shown in Figures 4, 5, 6. This includes labeling in anterior and posterior Cg/M2 (top left panels), the LP and Po nuclei of the thalamus (top right), area AL (middle right), as well as all layers of RSC and AM (bottom). Scale bars = 200μm.

Supplementary Table 1 | Animals and tracer injections

Injections in V1

Animal number	Sex	Weight (g)	Uni- or bilateral	Number of injections	Tracers in left hemisphere	Tracers in right hemisphere	Injection method	Plane of sectioning
74029	F	24	Bilateral	6	BDA: L-2.30, D-0.45 (6min) and 0.35 (4min) DA488: L-2.60, D-0.45 (6min) and 0.35 (4min) DA546: L-2.90, D-0.45 (6min) and 0.35 (4min) B: right in front of the tangential sinus	BDA: L+2.30, D-0.45 (6min) and 0.35 (4min) DA488: L+2.60, D-0.45 (6min) and 0.35 (4min) DA546: L+2.90, D-0.45 (6min) and 0.35 (4min) B: right in front of the tangential sinus	Ionotophoresis 6 µA, + current, 6s on/off for 10 min	Left tangential flattened, right coronal
74367*	F	24	Bilateral	6	BDA: L-2.30, D-0.45 (6min) and 0.35 (4min) DA488: L-2.60, D-0.45 (6min) and 0.35 (4min) DA546: L-2.90, D-0.45 (6min) and 0.35 (4min) B: right in front of the tangential sinus	BDA: L+2.30, D-0.45 (6min) and 0.35 (4min) DA488: L+2.60, D-0.45 (6min) and 0.35 (4min) DA546: L+2.90, D-0.45 (6min) and 0.35 (4min) B: right in front of the tangential sinus	Ionotophoresis 6 µA, + current, 6s on/off for 10 min	Left tangential flattened, right coronal
74368	F	23	Bilateral	6	DA488: L-2.30, D-0.45 (6min) and 0.35 (4min) DA546: L-2.60, D-0.45 (6min) and 0.35 (4min) BDA: L-2.90, D-0.45 (6min) and 0.35 (4min) B: right in front of the tangential sinus	DA488: L+2.30, D-0.45 (6min) and 0.35 (4min) DA546: L+2.60, D-0.45 (6min) and 0.35 (4min) BDA: L+2.90, D-0.45 (6min) and 0.35 (4min) B: right in front of the tangential sinus	Ionotophoresis 6 µA, + current, 6s on/off for 10 min	Left tangential flattened, right coronal
74572	F	24	Unilateral right hemisphere	3	-	DA488: L+2.30, D-0.45 (6min) and 0.35 (4min) DA546: L+2.60, D-0.45 (6min) and 0.35 (4min) BDA: L+2.90, D-0.45 (6min) and 0.35 (4min) B: right in front of the tangential sinus	Ionotophoresis 6 µA, + current, 6s on/off for 10 min	Coronal
74749**	F	27	Unilateral right hemisphere	3	-	DA488: L+2.30, D-0.45 (6min) and 0.35 (4min) DA546: L+2.60, D-0.45 (6min) and 0.35 (4min) BDA: L+2.90, D-0.45 (6min) and 0.35 (4min) B: right in front of the tangential sinus	Ionotophoresis 6 µA, + current, 6s on/off for 10 min	Coronal
53576***	F	30	-	-	-	-	-	Coronal

*representative case used for tangential flattened section in Figure 2
** representative case used for coronal sections of Figures 2 and 3 and Supplementary Figure 1
*** brain used for architectural delineations in Figure 1

Injections in PPC

Animal number	Sex	Weight (g)	Uni- or bilateral	Number of injections	Tracers in left hemisphere	Tracers in right hemisphere	Injection method	Plane of sectioning
72934*	M	25	Unilateral	3	-	DA546: L+1.25, D-0.60 (5 min) and 0.33 (5 min) DA488: L+1.63, D-0.60 (5 min) and 0.30 (5 min) DA647: L+2.00, D-0.60 (5 min) and 0.30 (5 min) B-1.90	Ionotophoresis 6 µA, + current, 6s on/off for 10 min	Coronal
72935	M	25	Unilateral	3	-	DA546: L+1.25, D-0.60 (5 min) and 0.35 (5 min) DA488: L+1.63, D-0.60 (5 min) and 0.35 (5 min) DA647: L+2.00, D-0.60 (5 min) and 0.35 (5 min) B-1.90	Ionotophoresis 6 µA, + current, 6s on/off for 10 min	Coronal
74574**	M	32	Bilateral	6	DA546: L-1.25, D-0.60 (6 min) and 0.35 (4 min) DA488: L-1.63, D-0.60 (6 min) and 0.35 (4 min) BDA: L-2.00, D-0.60 (6 min) and 0.35 (4 min) B-1.90	DA546: L+1.25, D-0.60 (6 min) and 0.35 (4 min) DA488: L+1.63, D-0.60 (6 min) and 0.35 (4 min) BDA: L+2.00, D-0.60 (6 min) and 0.35 (4 min) B-1.90	Ionotophoresis 6 µA, + current, 6s on/off for 10 min	Left tangential flattened, right coronal
75566***	M	31	Bilateral	6	DA546: L-1.25, D-0.60 (6 min) and 0.35 (4 min) DA488: L-1.63, D-0.60 (6 min) and 0.35 (4 min) BDA: L-2.00, D-0.60 (6 min) and 0.35 (4 min) B-1.90	DA546: L+1.25, D-0.60 (6 min) and 0.35 (4 min) DA488: L+1.63, D-0.60 (6 min) and 0.35 (4 min) BDA: L+2.00, D-0.60 (6 min) and 0.35 (4 min) B-1.90	Ionotophoresis 6 µA, + current, 6s on/off for 10 min	Left tangential flattened, right coronal
54611	M	29	Unilateral	1+1	-	AAVI.CamKII0.4.Cre.SV40 + AAV5-syn-FLEX-splitTVA-EGFP-B1G (helper virus) ENVA-psedotyped SAD-DeltaG-mCherry (rabies virus) B-1.90, L+1.50, D-0.50	Pressure. Nanoject. 200nl helper virus and 92 nl rabies virus	Coronal
54612	M	28	Unilateral	-	-	AAVI.CamKII0.4.Cre.SV40 + AAV5-syn-FLEX-splitTVA-EGFP-B1G (helper virus) ENVA-psedotyped SAD-DeltaG-mCherry (rabies virus) B-1.90, L+1.50, D-0.50	Pressure. Nanoject. 260nl helper virus and 92 nl rabies virus	Coronal
54845	M	28	Unilateral		-	AAVI.CamKII0.4.Cre.SV40 + AAV5-syn-FLEX-splitTVA-EGFP-B1G (helper virus) ENVA-psedotyped SAD-DeltaG-mCherry (rabies virus) B-2.00, L+1.50, D-0.50	Pressure. Nanoject. 200nl helper virus and 300 nl rabies virus	Coronal
54846****	M	27	Unilateral		-	AAVI.CamKII0.4.Cre.SV40 + AAV5-syn-FLEX-splitTVA-EGFP-B1G (helper virus) ENVA-psedotyped SAD-DeltaG-mCherry (rabies virus) B-2.00, L+1.50, D-0.50	Pressure. Nanoject. 200nl helper virus and 230 nl rabies virus	Coronal

* representative case used in Supplementary Figure 1
** representative case used in Supplementary Figure 3
*** representative case used for coronal and tangential flattened sections in Figures 4,5,6
**** representative case used in Figures 5 and 6

Supplementary Table 2 | Summary of nomenclatures for parietal and visual cortices in mice

Current paper	Paxinos & Franklin*	Wang & Burkhalter**	Allen Institute Connectivity map***
mPPC	MPtA	Anterior AM	Anterior VISam
lPPC	LPtA	A	VISa
PtP	PtPR/D	Anterior RL	Anterior VISrl
S1B	S1BF/S1	S1	SSp-bfd
RSC	-	-	RSP
RSG	A29c	-	RSPv
RSA	A30	RSA/RSD	RSPd
RSA	A30	MM	RSPagl
V2M	V2MM/ML	AM	VISam
V2M	V2MM/ML	PM	VISpm
V2L	V2L	RL	VISrl
V2L	V2L	AL	VISal
V2L	V2L	LM	VISl
V2L	V2L	LI	VISli
V2L	V2L	P	VISpl
V1	V1	V1	VISp
Te	TeA	LI	TEa

* Paxinos, G. & Franklin, K. (2012) *Paxinos' and Franklin's the Mouse Brain in Stereotaxic Coordinates*. Academic Press.

** Wang, Q. & Burkhalter, A. (2007) Area map of mouse visual cortex. *The Journal of comparative neurology*, **502**, 339-357.

*** https://scalablebrainatlas.incf.org/mouse/ABA_v3

Supplementary List 1 | Tracers, viruses and antibodies used in the study

- DA488: Dextran, Alexa Fluor™ 488; 10,000 MW, Anionic, Fixable, Thermo Fisher, Cat. No. D22910
- DA546: Dextran, Alexa Fluor™ 546; 10,000 MW, Anionic, Fixable, Thermo Fisher, Cat. No. D22911
- DA647: Dextran, Alexa Fluor™ 546; 10,000 MW, Anionic, Fixable, Thermo Fisher, Cat. No. D22914
- BDA: Dextran, Biotin, 10,000 MW, Lysine Fixable (BDA-10,000), Thermo Fisher Scientific Cat. No. D1956, RRID:AB_2307337
- AAV1.CamKII0.4.Cre.SV40, U. Penn Vector Core, Perelman School of Medicine, University of Pennsylvania
- AAV5-syn-FLEX-splitTVA-EGFP-B19G (Cliff Kentros lab)
- EnvA-pseudotyped SAD-DeltaG-mCherry (Cliff Kentros lab)
- Streptavidin, Alexa Fluor 633 conjugate, 1:400, Thermo Fisher Scientific Cat. No. S-21375, RRID:AB_2313500
- Rat anti-muscarinic acetylcholine receptor m2 monoclonal antibody, unconjugated, clone m2-2-b3, 1:750, Millipore Cat. No. MAB367, RRID:AB_94952
- Mouse anti-parvalbumin monoclonal antibody, unconjugated, clone PARV-19, 1:1000, Sigma-Aldrich Cat. No. P3088, RRID:AB_477329
- Anti-rat IgG (H+L), mouse adsorbed, made in rabbit antibody, 1:300, Vector Laboratories Cat. No. BA-4001, RRID:AB_10015300
- Goat anti-mouse IgG, biotin conjugated, 1:200, Sigma-Aldrich Cat# B7151, RRID:AB_258604
- Rabbit RFP Antibody Pre-adsorbed, 1:1000, Rockland Cat. No. 600-401-379, RRID:AB_2209751
- Chicken anti-GFP, 1:500, Abcam Cat. No. ab13970, RRID:AB_300798
- F(ab)2-goat anti-rabbit IgG (H+L) cross-adsorbed, Alexa Fluor 546, 1:1000, Thermo Fisher Scientific Cat. No. A-11071, RRID:AB_2534115
- Goat anti-chicken IgY H&L, Alexa Fluor® 488, 1:1000, Abcam Cat. No. ab150169, RRID:AB_2636803